Chapter Three

Magnetic Integration for Multiphase VRMs

Integrated magnetic components are used in multiphase VRMs in order to reduce the number of the magnetics and to improve efficiency. All the magnetic components can be integrated into a single core, in which the windings are wound around the center leg and the air gaps are placed on the two outer legs. However, the core structure requires precise adjustment and is not mechanically stable. The existence of air gaps on the two outer legs causes EMI issues. Large leakage inductance in the integrated magnetics causes severe parasitic ringing, decreases duty cycle and impairs efficiency.

To solve these problems, this chapter proposes a novel magnetic integration approach. In the proposed structure, all the windings are wound on the two outer legs, the core structure has an air gap in the center leg, and there are no air gaps in the two outer legs. This kind of core is easier to manufacture. The windings are physically located on the same legs and the leakage inductance can thus be minimized. The air gap in the center leg introduces inverse coupling between the two output inductors. Both the steady-state and dynamic performances of the converter can be improved. Both the core loss and winding loss can also be reduced because of the flux ripple cancellation in the center leg.

Unlike conventional magnetic integrations, the input filter can also be integrated into the integrated magnetic structure. In the proposed structure, the input inductor is formed by the leakage inductance between the transformer's primary windings. This leakage can be controlled by carefully designing windings. With the proposed integrated magnetics, it is possible to use only a single magnetic core for the whole converter.

3.1. INTRODUCTION

Multiphase converters require many magnetic components, which may increase the cost and size of the VRM. Integrated magnetics can reduce the number of the magnetic components. Besides this, integrated magnetics can also reduce the core loss. It has been demonstrated that a 1% to 2% efficiency improvement can be achieved by using integrated inductors in the multiphase buck converter [C19, C24]. By coupling inductors between the channels, integrated magnetics can further reduce the steady-state current ripple while maintaining the same transient response. The efficiency of the VRM can be improved by an additional 3% [C21, C22].

In this chapter, the use of integrated magnetics to reduce the number of magnetic components and to further improve the efficiency is explored for both the 12V and the 48V VRMs.

Figure 3.1 shows the multiphase coupled-buck converter, which is proposed in Chapter 2 and which has been proven to be a very promising topology for 12V VRMs.

As shown in Figure 3.1, a high number of magnetic components used are used in this topology. Each channel has a three-winding coupled inductor.

The proposed multiphase coupled-buck converter can also be used for 48V VRMs with a suitable turns ratio if there is no isolation requirement. However, isolation is often required for 48V VRMs that are used in distributed power systems.

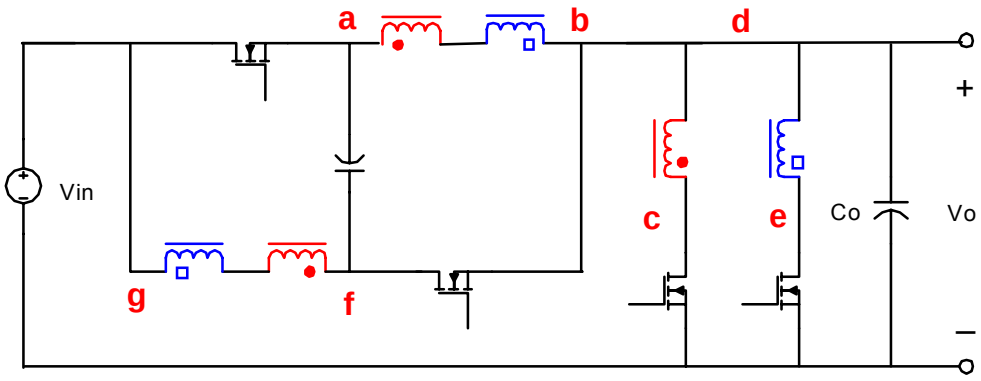

Figure 3.1. Multiphase coupled-buck converter for 12V VRM.

Recent research indicates that the symmetrical half-bridge topology with the current doubler and synchronous rectifier is a suitable approach for 48V VRMs [B34]. A topology called the push-pull forward converter was proposed recently, as shown in Figure 1.16. It offers an improved transient response and increased package density. Experimental results indicate that the push-pull forward topology can demonstrate 3% better efficiency than either a symmetrical or an asymmetrical half-bridge converter [A15, B36]. As discussed in Chapter 2, this topology is essentially the isolated counterpart of the multiphase coupled-buck converter.

The integration of the magnetic components will be addressed for both the multiphase coupled-buck converter and the push-pull forward converter with the current-doubler rectifier. Although the schematics of the magnetic components are quite different in these topologies, their integrated magnetic structures are the same, as will be discussed in the next section.

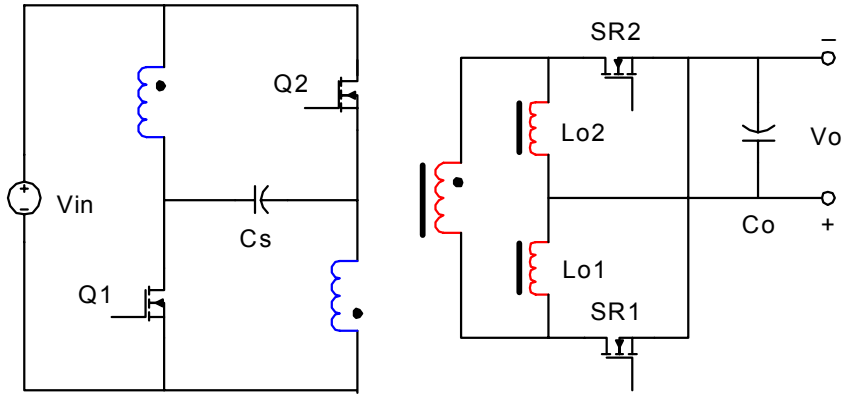

Figure 3.2. Push-pull forward converter with current-doubler rectifier.

3.2. INTEGRATED MAGNETICS FOR MULTIPHASE VRMS

3.2.1. Integrated Magnetics for 12V VRM

In the multiphase coupled-buck converter, the configuration of the magnetic components and associated output stage can be extracted and redrawn as shown in Figure 3.3(a). In order to simplify the drawing, Figure 3.3(a) only shows one high-turns winding. The same discussion can be applied to two or more high-turns windings.

Figure 3.3(b) shows the discrete magnetic implementation for Figure 3.3(a)'s circuit. The two coupled inductors are built on two pairs of separate U-I cores. The air gaps are placed on one leg of the U-I cores, as shown in Figure 3.3(b).

The two pairs of U-I cores can then be moved together and combined into a pair of E-I cores, as shown in Figure 3.3(c). There is no air gap in the center leg of the E-I cores. The center leg is a low-reluctance path. The fluxes generated by the two windings in the two outer legs all flow through the center leg. There is no interaction between the two flux loops. Although the two inductors are built on the same pair of E-I cores, there is no coupling effect between them. The core structure is thus simplified.

The winding structure can also be simplified. As shown in Figure 3.3(d), the two high-turns windings can be moved from the two outer legs to the center leg due to the flux continuity. The resulting structure actually is the integrated magnetics structure proposed by W. Chen [C19, C24]. Both core and winding integration are realized in this structure. For high-current applications, this winding integration becomes more important because of its lower interconnection and conduction losses.

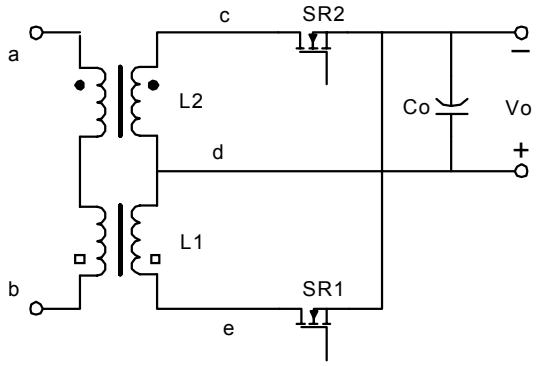

(a)

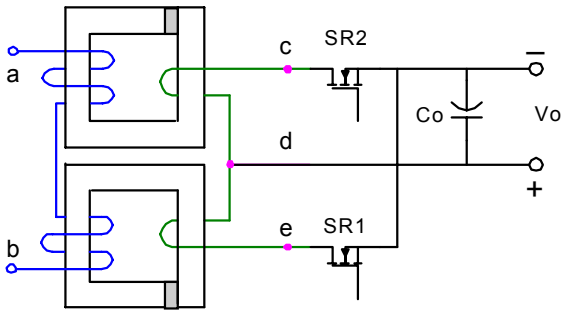

(b)

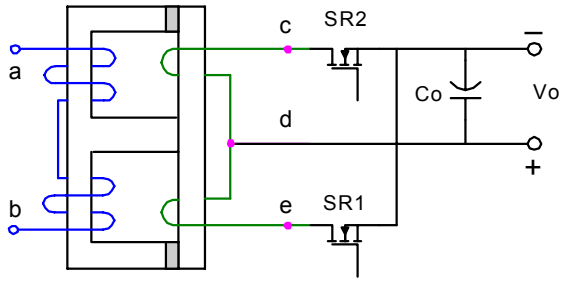

(c)

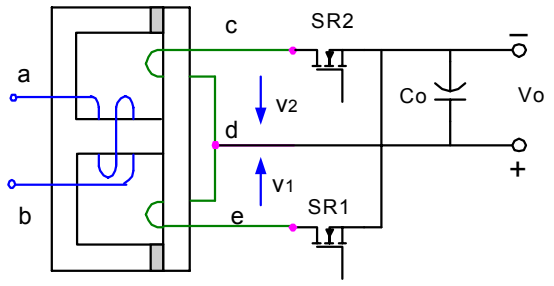

(d)

Figure 3.3. (a) The magnetics in the multiphase coupled-buck converter; (b) discrete magnetic implementation; (c) core simplification; and (d) winding simplification (W.Chen's integrated magnetics [C26]).

3.2.2. Integrated Magnetics for 48V VRM

The configuration of magnetic components in the push-pull forward converter forms the current-doubler structure, as shown in Figure 3.2. The current-doubler rectifier is the most popular secondary topology for low-voltage high-current applications. It consists of

one transformer and two output inductors. The transformer and two output inductors in the current-doubler rectifier can be combined into a single EE or EI core.

Figure 3.4 shows the schematic of the current-doubler rectifier and its discrete magnetic implementation, as well as several existing integrated magnetic implementations.

Figure 3.4(a) shows the schematic of the current-doubler rectifier. To simplify the following discussion, only one primary winding is drawn. The same discussion can be applied to cases with two or more primary windings, such as in the push-pull forward topology.

Figure 3.4(b) shows the discrete magnetic implementation for the current-doubler rectifier. Three magnetic cores, three high-current windings and five high-current interconnections are needed.

Figure 3.4(c) shows the integrated magnetic structure proposed by O. Seiersen [C15, C16]. A single conventional EE or EI core is used with air gaps in the outer legs only. The implementation may reduce the overall size of the magnetics, since the transformer and two inductors share the outer legs of the core. It is important to note that this magnetic integration focuses only on core integration while neglecting winding integration. Three high-current windings and five high-current interconnections are still needed.

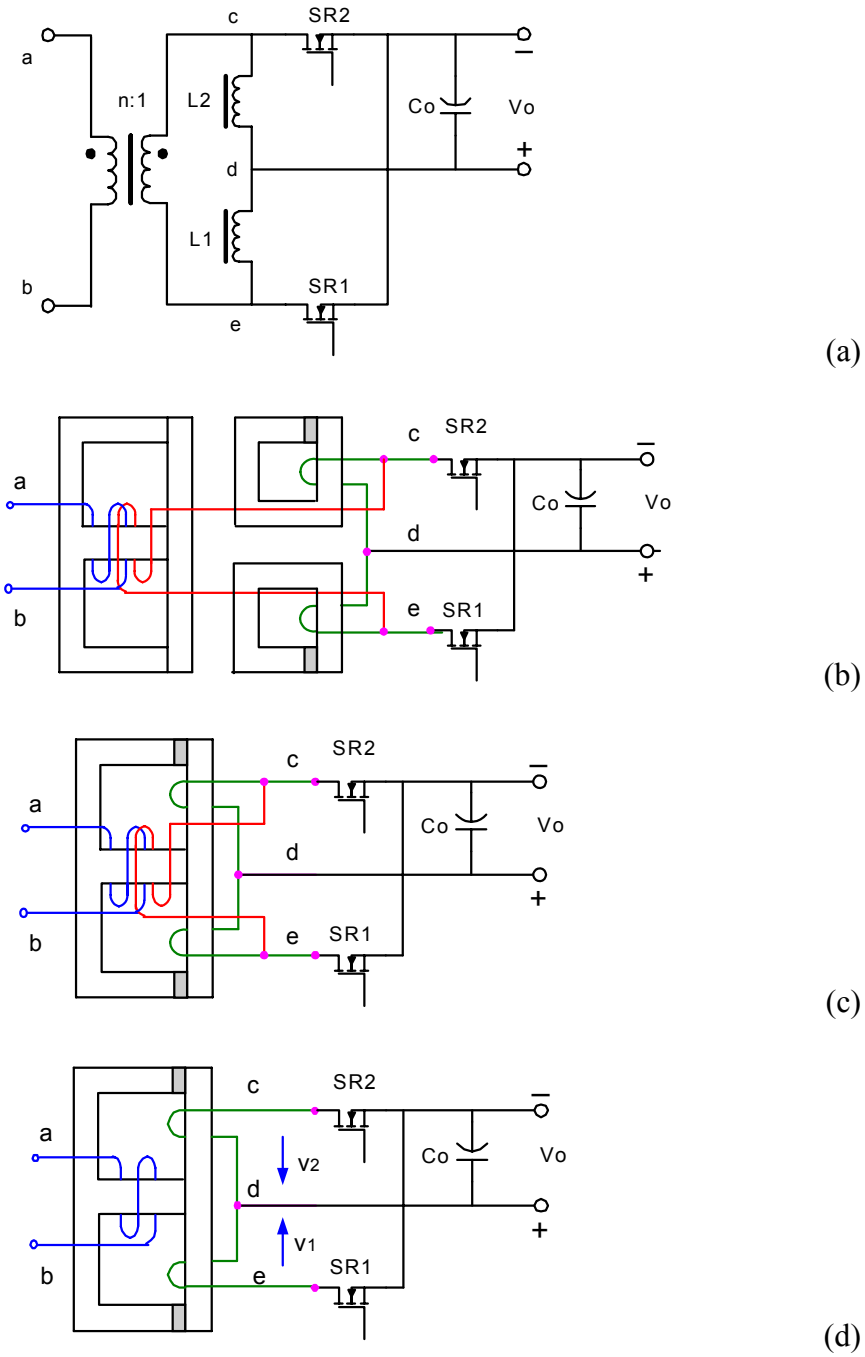

Figure 3.4. (a) Current-doubler rectifier; (b) discrete magnetic implementation; (c) O. Seiersen's integrated magnetics [C15, C16]; and (d) W. Chen's integrated magnetics [C26].

Figure 3.4(d) shows an improved integrated magnetic structure proposed by W. Chen [C26]. Both core and winding integration are realized in this structure. Not only do the transformer and two inductors share the outer legs of the core, but the transformer secondary winding and inductor windings are also integrated together. Only two high-current windings and three high-current interconnections are needed. For high-current applications, this winding integration becomes more important because of its lower interconnection and conduction losses. As a result, this integrated magnetic structure allows for lower overall system cost and size, as well as higher efficiency.

3.2.3. Limitations of Integrated Magnetics

As can be seen from Figures 3.3(d) and 3.4(d), the integrated magnetic structures are the same for both the multiphase coupled-buck converter and the push-pull forward converter with the current-doubler rectifier. Despite all the advantages described in the proceeding sections, this integrated magnetic structure also has some drawbacks.

Figure 3.5 illustrates the core structure of the integrated magnetics, with only one winding shown for simplification. The air gaps are placed on the two outer legs and there is no air gap in the center leg in order to prevent interaction between the two flux loops. However, this kind of magnetic core is not a standard industry practice; the precise gapping adjustment and filling are requested, which means mass production is difficult and costly. Besides the cost, the two pieces of core are connected only at the center leg, rendering the structure mechanically unstable. Moreover, the existence of air gaps on the two outer legs also causes EMI issues.

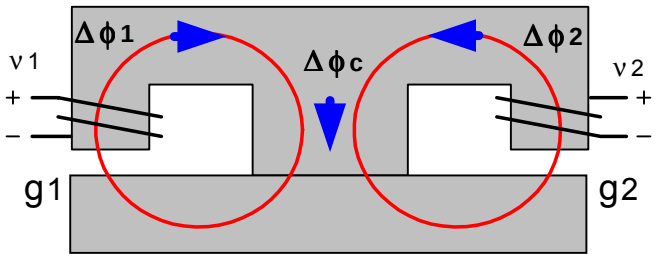

Figure 3.5. Core structure of the existing integrated magnetics.

Another drawback is that the transformer in the existing integrated magnetics has a large leakage inductance. As shown in Figure 3.6, the transformer's primary windings are wound around the center leg while the transformer's secondary windings are wound on the two outer legs. A significant leakage flux exists in the transformer windings, and the coupling between the transformer's primary and secondary windings is poor. This causes the transformer's large leakage inductance, which in turn causes severe parasitic ringing across the semiconductor devices, a decrease in the effective duty cycle at the secondary, and an overall impairment of efficiency.

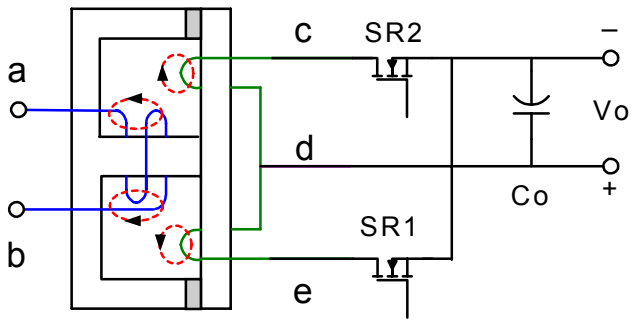

Figure 3.6. Large leakage flux in the existing integrated magnetics.

Figure 3.7 shows the tested waveforms corresponding to the push-pull forward converter using the integrated magnetic structure shown in Figures 3.3(d) and 3.4(d). The test conditions are V_{IN}=48 V, V_O=1.2 V, I_O=70 A, and F_S=100 KHz. Because of the large leakage inductance, severe parasitic ringing is observed on the drain-source voltage waveforms of the primary switches. The loss of the effective duty cycle at the secondary can also be seen from the drain-source voltage waveform of the secondary switches. The duty cycle loss is more than 10%.

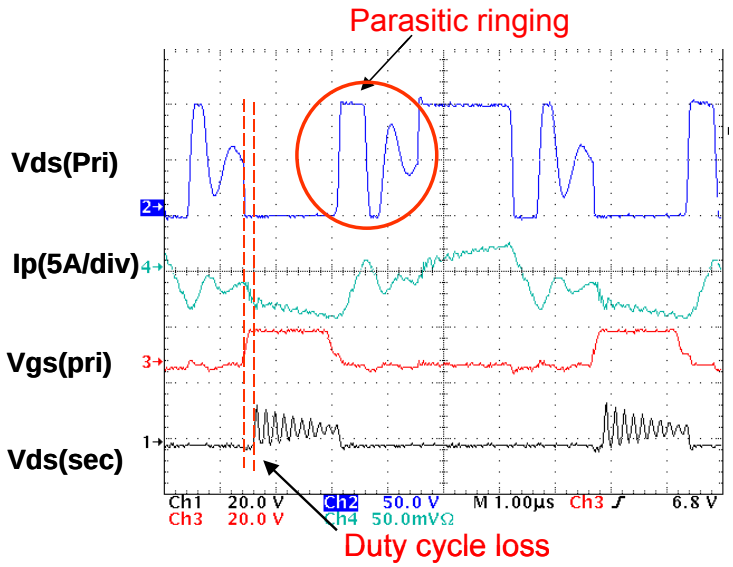

Figure 3.7. Test waveforms of the existing integrated magnetics.

3.3. AN IMPROVED INTEGRATED MAGNETICS

In order to overcome the limitations of the existing structure, a novel integrated magnetics is proposed in this section.

In the proposed structure, the core structure requires an air gap in the center leg and no air gap in the two outer legs, which is easier to manufacture. All the windings are wound on the two outer legs so that the leakage inductance can be minimized. The flux ripples are canceled in the center leg. With the small flux ripples in the center leg, both the core loss and the winding loss can also be reduced. The air gap in the center leg introduces inverse coupling between the two output inductors. Both the steady-state and dynamic performances of the converter can be improved.

3.3.1. Derivation and Analysis of Improved Integrated Magnetics

Figure 3.8 shows the approach for deriving the improved integrated magnetic structure. The discussion begins with the existing integrated magnetic structure shown in Figure 3.4(d).

Step 1: The transformer's primary winding is split between the two outer legs, as shown in Figure 3.8(b), without changing the flux distributions. Since both the primary and secondary windings are wound on the two outer legs, interleaving can be used to minimize the leakage inductance of the integrated transformer.

Step 2: The polarity of one set of windings is changed through different winding connections, as shown in Figure 3.8(c). Correspondingly, the direction of flux is changed as well. Before the change, the DC flux circulates between the two outer legs, and no DC flux exists in the center leg. The air gaps on the outer legs prevent saturation of the core. After the polarity change, no DC flux circulates between the two outer legs.

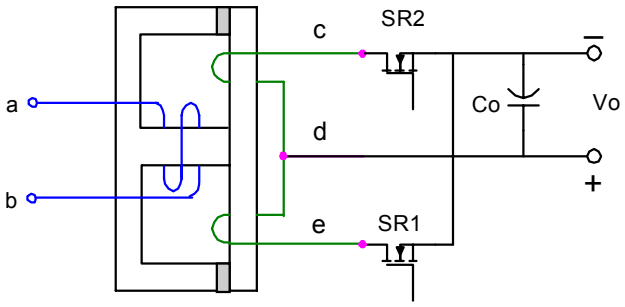

(a)

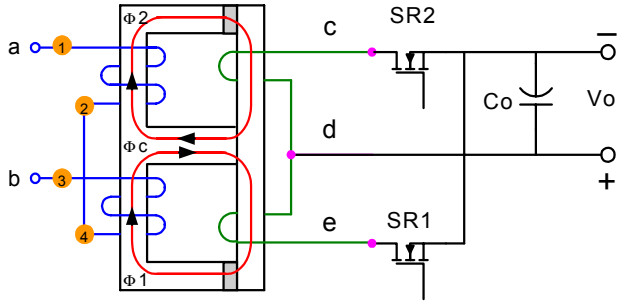

(b)

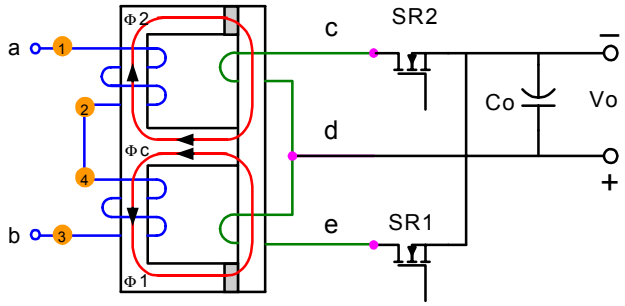

(c)

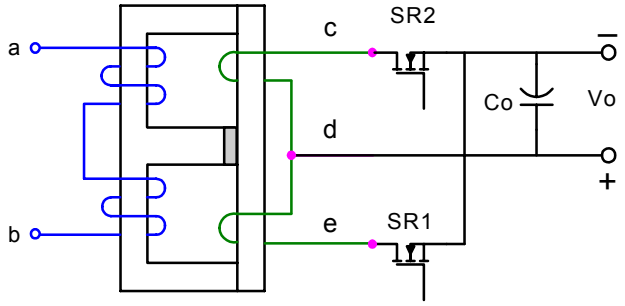

(d)

Figure 3.8. Derivation of the improved integrated magnetic structure: (a) Original structure, (b) winding splitting, (c) polarity change, and (d) gap shifting.

Step 3: As shown in Figure 3.8(c), since there is no DC flux circulating between the two outer legs, the air gaps in the outer legs can be shifted to the center leg while keeping the core unsaturated, as shown in Figure 3.8(d).

Figure 3.8(d) shows the proposed integrated magnetic structure, in which the transformer's primary and secondary windings are wound on the two outer legs. Thus, the integrated transformer offers minimized leakage inductance. Moreover, the core structure has an air gap in the center leg and no air gaps in the outer legs; this is the standard industry practice and is much easier to manufacture.

Figure 3.9 shows the reluctance model for the proposed magnetic circuit, which consists of two parts: the reluctance of the magnetic path and the representation of the windings. In Figure 3.9, the windings are represented as the magnetomotive force (MMF) sources. The R_O and R_C represent the reluctance of the outer and center legs, respectively. The major flux directions are determined by using the Right-Hand Rule, and the leakage flux paths are not considered.

From the magnetic reluctance circuit shown in Figure 3.9, the fluxes in the cores can be derived in the form of reluctances and MMF sources, as follows:

$$\begin{aligned} \varphi 1 &= \frac{Rc + Ro}{Ro \cdot (Ro + 2 \cdot Rc)} \cdot Ns \cdot i_{L1} - \frac{Rc}{Ro \cdot (Ro + 2 \cdot Rc)} \cdot Ns \cdot i_{L2} \\ \varphi 2 &= -\frac{Rc}{Ro \cdot (Ro + 2 \cdot Rc)} \cdot Ns \cdot i_{L1} + \frac{Rc + Ro}{Ro \cdot (Ro + 2 \cdot Rc)} \cdot Ns \cdot i_{L2} \end{aligned} \quad . \tag{3.1}$$

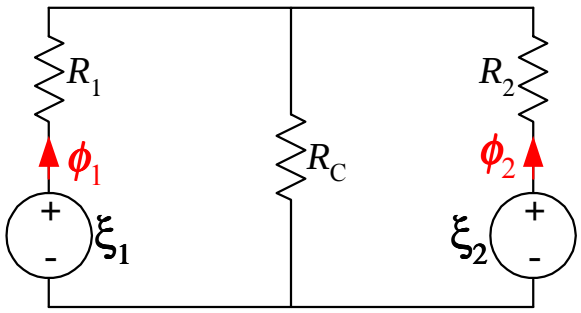

Figure 3.9. Magnetic reluctance circuit of proposed integrated magnetics.

The electrical circuit model can be easily derived from the magnetic analog model, using the principle of duality. The equivalent electrical circuits of the proposed integrated magnetic circuit are shown in Figure 3.10. The equivalent circuit can be represented by either the coupled inductors, as shown in Figure 3.10(a), or the transformer and the inductors, as shown in Figure 3.10(b). These two equivalent circuits are interchangeable. Figure 3.10(b)'s circuit is the current-doubler rectifier with the two output inductors reverse-coupled. This circuit will be used for the following discussion.

Assuming L1=L2=L, and that the mutual inductance between L1 and L2 is M, Figure 3.10 shows that the relationship between voltage and current can be derived as follows:

$$\begin{aligned} v_1 &= (L+M)\cdot\frac{di_{L1}}{dt} - M\cdot\frac{di_{L2}}{dt} \\ v_2 &= -M\cdot\frac{di_{L1}}{dt} + (L+M)\cdot\frac{di_{L2}}{dt} \end{aligned} \quad . \tag{3.2}$$

The voltages across the corresponding windings relate to the flux in the cores where the windings are wound, as follows:

$$\begin{aligned} v_1 &= N_S \cdot \frac{d\varphi 1}{dt} \\ v_2 &= N_S \cdot \frac{d\varphi 2}{dt} \end{aligned} \quad . \tag{3.3}$$

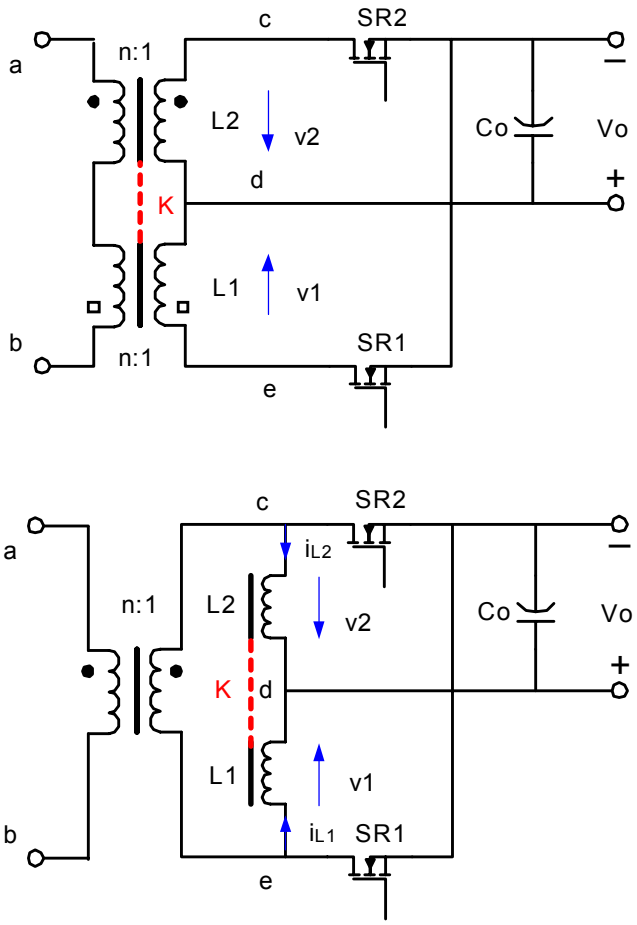

Figure 3.10. Equivalent electrical circuits of proposed integrated magnetic circuit: (a) in the form of coupled inductors, and (b) in the form of the transformer and the inductors.

Substituting Equations 3.1 and 3.2 into Equation 3.3, the analytical relationship between inductances and reluctances can be derived as follows:

$$\begin{aligned} L &= \frac{Ns^2 \cdot (Ro + Rc)}{Ro \cdot (Ro + 2 \cdot Rc)} \\ M &= \frac{Ns^2 \cdot Rc}{Ro \cdot (Ro + 2 \cdot Rc)} \end{aligned} . \tag{3.4}$$

The coupling coefficient of the two coupled inductors can be further derived as follows:

$$k = \frac{M}{L} = \frac{Rc}{Ro + Rc} . \tag{3.5}$$

In the proposed integrated magnetics, only the center leg has an air gap, and there are no air gaps in either of the two outer legs. The reluctance in the center leg is much larger than those of the outer legs ($Rc >> Ro$). Equations 3.4 and 3.5 can be simplified as follows:

$$\begin{aligned} L &\approx \frac{Ns^2}{2 \cdot Ro} \\ M &\approx \frac{Ns^2}{2 \cdot Ro} \\ k &= \frac{M}{L} \approx 1 \end{aligned} . \tag{3.6}$$

As can be seen from Equation 3.6, without considering the reluctance from the magnetic material, the coupling coefficient for the two inductors in the proposed structure is close to one. However, the concept of unity coupling is very different from conventional ideas. “Close to one” does not mean “equal to one.” The increase in the coupling coefficient is achieved by the increase in both the self- and mutual inductances.

The two coupled inductors still have a certain amount of leakage inductance. In practice, the reluctance components from the magnetic material can influence the value of Ro and Rc, and the typical coupling coefficient k is in the range of 0.8 to 0.9.

With the understanding of the relationship between the integrated magnetic circuit and the equivalent electrical circuit, the following section discusses the flux distributions in the proposed integrated magnetics and the design of the magnetic core.

Figure 3.11 shows the AC fluxes in the core of the proposed integrated magnetics. According to Farad's Law, the AC fluxes in the two outer legs, $\Delta\phi 1$ and $\Delta\phi 2$, are the time integral of the voltage (which is more simply stated as volt-seconds) across the corresponding winding. For both the existing and the proposed integrated magnetics, the winding voltage waveforms are the same because they are determined by the conduction states of the external switches. The magnitude of the AC fluxes in the two outer legs can be derived by the time integral of Equation 3.3, as follows:

$$\Delta\varphi 1 = \Delta\varphi 2 = \frac{Vo \cdot (1 - D)}{Ns \cdot Fs}. \tag{3.7}$$

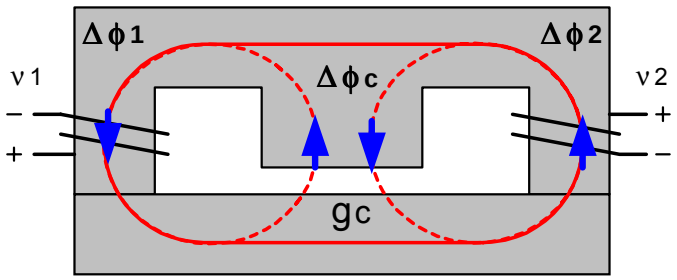

Figure 3.11. AC fluxes in the core of proposed integrated magnetics.

The AC flux in the center leg is the sum of the AC fluxes in the two outer legs. In the existing integrated magnetics, as shown in Figure 3.5, the AC fluxes are added in the center leg according to the phase relationship of winding voltages v1 and v2. However, in the proposed structure, the polarity of one set of windings is changed; therefore, the direction of AC flux in one of the two outer legs is also changed. Consequently, the AC fluxes are canceled in the center leg. The magnitude of AC flux in the center leg for both the existing and the proposed structure are derived as follows:

$$\begin{cases} \Delta\varphi c = \dfrac{Vo \cdot (1 - 2D)}{Ns \cdot Fs} \text{ in the proposed structure, and} \\ \Delta\varphi c = \dfrac{Vo}{Ns \cdot Fs} \text{ in the existing structure.} \end{cases} . \tag{3.8}$$

With the reduction of the magnitude of AC flux in the center leg, the proposed integrated magnetics has a lower core loss in the center leg than do existing integrated magnetics.

Another advantage of the AC flux cancellation in the center leg is the much smaller fringing effects and fewer EMI problems caused by the air gap. Large air gaps are usually associated with fringing effects and EMI problems. However, the AC flux through the air gap in the center leg is much smaller. The fringing effects associated with the center leg air gap are much smaller. The fewer the eddy currents generated in the windings, the lower the winding loss will be.

Another important factor in integrated magnetic design is the DC flux bias in the different legs of the core.

Substituting DC components into Equation 3.2, the DC flux bias in the core of the proposed integrated magnetics can be derived as:

$$\begin{aligned}\Phi 1 &= \frac{Rc + Ro}{Ro \cdot (Ro + 2 \cdot Rc)} \cdot Ns \cdot I_{L1} - \frac{Rc}{Ro \cdot (Ro + 2 \cdot Rc)} \cdot Ns \cdot I_{L2} \\ \Phi 2 &= -\frac{Rc}{Ro \cdot (Ro + 2 \cdot Rc)} \cdot Ns \cdot I_{L1} + \frac{Rc + Ro}{Ro \cdot (Ro + 2 \cdot Rc)} \cdot Ns \cdot I_{L2}\end{aligned} . \tag{3.9}$$

With the definitions of self-inductance and mutual inductance M, Equation 3.9 can be rewritten in the format of inductances, as follows:

$$\begin{aligned}\Phi 1 &= \frac{L \cdot I_{L1}}{Ns} - \frac{M \cdot I_{L2}}{Ns} \\ \Phi 2 &= -\frac{M \cdot I_{L1}}{Ns} - \frac{L \cdot I_{L2}}{Ns}\end{aligned} . \tag{3.10}$$

Assuming the two inductors have the same DC currents (I_L=I_{L1}=I_{L2}), Equations 3.9 and 3.10 can be simplified as:

$$\Phi 1 = \Phi 2 = \frac{Ns \cdot I_L}{Ro + 2 \cdot Rc} = \frac{(L - M) \cdot I_L}{Ns} . \tag{3.11}$$

With the assumption $Rc >> Ro$, Equation 3.11 can be further simplified as:

$$\Phi 1 = \Phi 2 = \frac{Ns \cdot I_L}{2 \cdot Rc} = \frac{(L - M) \cdot I_L}{Ns} . \tag{3.12}$$

For the proposed integrated magnetics, the DC flux in the center leg is the sum of the DC fluxes in the two outer legs. The cross-section area of the center leg of conventional

EE or EI cores is double those of the outer legs. In the proposed integrated magnetics, the three legs have equal DC flux biases.

As a comparison, the DC flux bias in the core of the existing integrated magnetics is also derived, following a manipulation similar to that shown in Equation 3.12:

$$\Phi 1 = \Phi 2 = \frac{Ns \cdot I_L}{Ro} = \frac{L \cdot I_L}{Ns}. \qquad (3.13)$$

In the existing integrated magnetic structure, the DC flux in the center leg is zero. However, zero DC flux does not mean that the cross section of the center leg can be reduced. In contrast, the AC flux in the center leg is so large that the cross-section area is mainly determined by the core loss in the center leg.

According to Equations 3.12 and 3.13, with the same value for L-M (M=0 in the existing structure), the existing and proposed integrated magnetic structures have equal DC flux biases in the two outer legs. Assuming that the cross-section area of the center leg is twice that of each outer leg, the use of the same length of air gap in the existing and proposed structures achieves equal DC fluxes in the two outer legs. The reason to choose the same value for L-M is to ensure that the two magnetic circuits retain the same output current ripples and transient inductor slew rates. The value L-M is defined as the transient equivalent inductance Leq2.

For the proposed integrated magnetic structure, the self-inductance is larger than that of the existing structure. Larger inductances usually result in larger DC fluxes if the same

cores and windings are used. However, the DC fluxes in the outer legs are the same for both the existing and the proposed structures. This can be explained briefly by Figure 3.12.

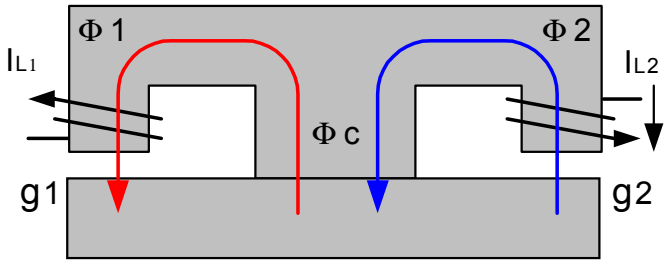

(a)

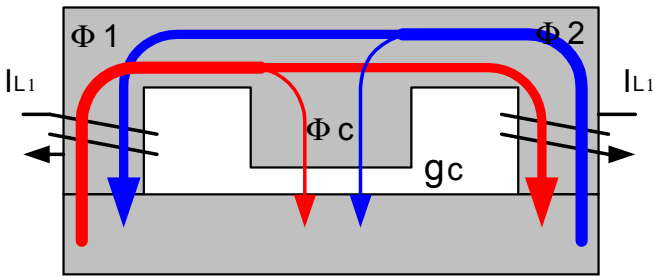

(b)

Figure 3.12. DC flux bias in the core structures of: (a) the existing integrated magnetics, and (b) the proposed integrated magnetics.

In the existing structure, the DC fluxes generated by the two sets of windings do not affect each other, as shown in Figure 3.12(a). For the proposed structure, the majority of the DC flux generated by one set of windings goes through the other set. Because of the inverse direction, the majority of DC flux in the two outer legs is cancelled; the percentage of the DC flux that is cancelled is proportional to the mutual inductance. Although a larger self-inductance in the proposed structure generates larger DC flux, the

percentage of the cancelled DC flux is also increased. The overall effect is that the net DC fluxes in the outer legs are the same as those in the existing structure. The net DC fluxes in the outer legs go through the center leg.

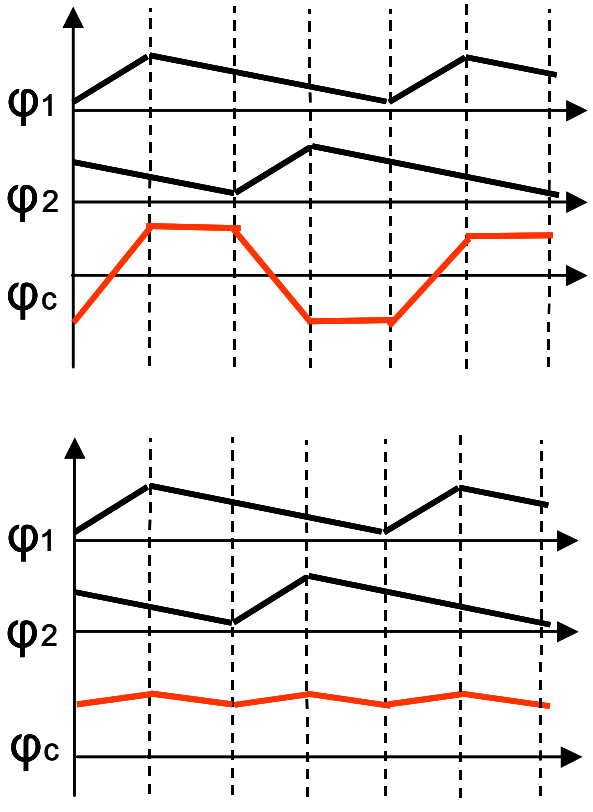

Figure 3.13. Flux waveforms: (a) in the existing integrated magnetics, and (b) in the proposed integrated magnetics.

In summary, the flux distribution in the core structures can be illustrated in Figure 3.13 for both the existing and proposed integrated magnetics. If the same cores and windings are used, the existing and proposed integrated magnetic structures have the same AC fluxes in the two outer legs. If the two core structures are designed to have the same transient equivalent inductances, the DC fluxes in the two outer legs are the same,

too. In the center leg of the existing structure, the AC fluxes are added, and the DC fluxes are canceled to zero; for the proposed structure, the AC fluxed are canceled, and the DC fluxes are added.

3.3.2. Inductor Coupling Effect and Its Influence on Converter Performance

The air gap in the center leg introduces coupling between the two output inductors in the proposed integrated magnetic circuit. This section discusses the influences of this coupling on the performance of the converter.

The effect of coupled inductors is illustrated by the use of the equivalent electrical circuit shown in Figure 3.10. The two inductors are inversely coupled.

The relationship between the voltages and currents of the two coupled inductors, as shown in Figure 3.10, can be described as follows:

$$\begin{bmatrix} v_1 \\ v_2 \end{bmatrix} = \begin{bmatrix} L & -M \\ -M & L \end{bmatrix} \cdot \begin{bmatrix} \frac{di_{L1}}{dt} \\ \frac{di_{L2}}{dt} \end{bmatrix}. \tag{3.14}$$

For the existing integrated magnetic circuit, the two inductors are non-coupled (M=0), and the corresponding equations are as follows:

$$\begin{bmatrix} v_1 \\ v_2 \end{bmatrix} = \begin{bmatrix} L & 0 \\ 0 & L \end{bmatrix} \cdot \begin{bmatrix} \frac{di_{L1}}{dt} \\ \frac{di_{L2}}{dt} \end{bmatrix}. \tag{3.15}$$

In order to directly see the effect of inductor coupling on converter performance, the concept of equivalent inductance is adopted. This concept is proposed by Pitleong Wong [C21, C22] and is used to analyze the coupled inductors in two-phase buck converter. The concept is described briefly as follows:

Using simple mathematical manipulation, the coupled-inductor format shown in Equation 3.14 can be rewritten in a non-coupled inductor format, as follows:

$$\begin{bmatrix} v_1 + \frac{M}{L} \cdot v_2 \\ v_2 + \frac{M}{L} \cdot v_1 \end{bmatrix} = \begin{bmatrix} L - \frac{M^2}{L} & 0 \\ 0 & L - \frac{M^2}{L} \end{bmatrix} \cdot \begin{bmatrix} \frac{di_{L1}}{dt} \\ \frac{di_{L2}}{dt} \end{bmatrix}. \tag{3.16}$$

If the relationship between v_1 and v_2 can be found, the two inductors can be decoupled and Equation 3.16 can be simplified, as follows:

$$\begin{bmatrix} v_1 \\ v_2 \end{bmatrix} = \begin{bmatrix} Leq & 0 \\ 0 & Leq' \end{bmatrix} \cdot \begin{bmatrix} \frac{di_{L1}}{dt} \\ \frac{di_{L2}}{dt} \end{bmatrix}. \tag{3.17}$$

In Equation 3.17, the inductances Leq and Leq' are defined as the equivalent inductances. The purpose of the equivalent inductances is to mathematically decouple the coupled inductors, so that they are comparable to non-coupled inductors. The relationship between v1 and v2 may be different during each time interval in a switching cycle, and the corresponding equivalent inductances also vary within a switching cycle.

In the following explanation, the concept of equivalent inductance is used to investigate the effect of inductor coupling on converter performance.

Figure 3.14 shows the waveforms of v_1 and v_2 in the proposed integrated magnetic circuit. There are two possible voltage values for v_1 and v_2: Va, corresponding to both switches SR1 and SR2 being on; and Vb, corresponding to one switch being on and the other switch being off. The relationship between Va and Vb can be found as follows:

$$D \cdot Va = -(1-D) \cdot Vb = -D' \cdot Vb \,. \tag{3.18}$$

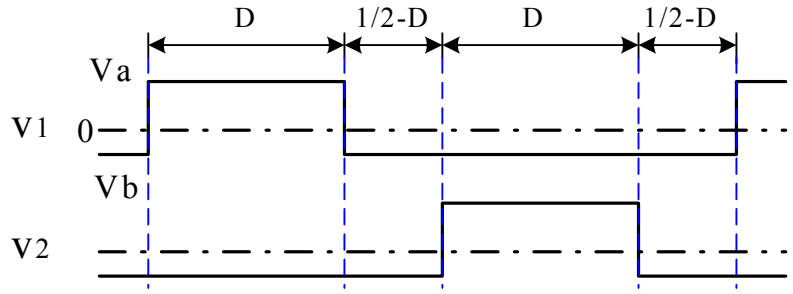

Figure 3.14. Voltage waveforms across two coupled inductors.

There are four time intervals within one switching cycle. The relationships between v_1 and v_2 are different in each time interval.

During (t0-t1), switch SR1 is on and switch SR2 is off (v_1=Va and v_2=Vb). The relationship between voltages v_1 and v_2 can be determined from Equation 3.18 as follows:

$$v_1 = -\frac{D'}{D} v_2 \,. \tag{3.19}$$

Substituting Equation 3.19 into Equation 3.16, the voltage and current relationship of the two coupled inductors can be described in the decoupled format, as follows:

$$\begin{bmatrix} v_1 \\ v_2 \end{bmatrix} = \begin{bmatrix} \dfrac{L-\dfrac{M^2}{L}}{1-\dfrac{M}{L}\cdot\dfrac{D}{D'}} & 0 \\ 0 & \dfrac{L-\dfrac{M^2}{L}}{1-\dfrac{M}{L}\cdot\dfrac{D'}{D}} \end{bmatrix} \cdot \begin{bmatrix} \dfrac{di_{L1}}{dt} \\ \dfrac{di_{L2}}{dt} \end{bmatrix}. \tag{3.20}$$

Equation 3.20 has the same format as Equation 3.17. By comparing these two equations, the equivalent inductances can be found. For simplification, only the equivalent inductance in the first phase, corresponding to coupled inductor L1, is discussed. The equivalent inductance in the second phase, corresponding to coupled inductor L2, is similar except for a phase shift. For the first phase, the equivalent inductance in the time interval (t0-t1) is as follows:

$$Leq1 = \frac{L^2 - M^2}{L - \dfrac{D}{D'}\cdot M}. \tag{3.21}$$

Similarly, for the other three time intervals, the relationship between voltages v_1 and v_2 can be determined using Equation 3.18. By substituting the relationship between the two inductor voltages into Equation 3.16, the equivalent inductances can be derived for each time interval within a switching cycle.

The equivalent inductance for the first phase during time interval (t1-t2) can be defined as:

$$Leq2 = L - M . \tag{3.22}$$

The equivalent inductance for the first phase during time interval (t2-t3) can be derived as:

$$Leq3 = \frac{L^2 - M^2}{L - \frac{D'}{D} \cdot M} . \tag{3.23}$$

During time interval (t3-t4), the voltages applied to the two inductors are exactly the same as during time interval (t2-t3). Thus, the equivalent inductance in this time interval should be equal to Leq2. So, there are three different equivalent inductances in each switching cycle.

In the preceding discussion, the relationship between the two inductor voltages is derived by the use of the steady-state duty cycle D. During transient responses, the duty cycle is changing. However, the two possible voltages applied to the inductors are still the same as under the steady-state conduction if the small transient voltage deviations are ignored. Thus, the equivalent inductances are still valid during transient responses.

Based on the preceding equivalent inductance discussion, the following section analyzes the effects of the coupling inductors on converter performance, both in steady-state operations and during transient responses. The steady-state criterion is the current

ripple because it has a direct impact on converter efficiency. The transient criterion is the current slew rate during transient responses.

Figure 3.15 shows the inductor voltage and current waveforms during the transient for the non-coupling and coupling cases. The inductor voltage waveforms for both cases are the same.

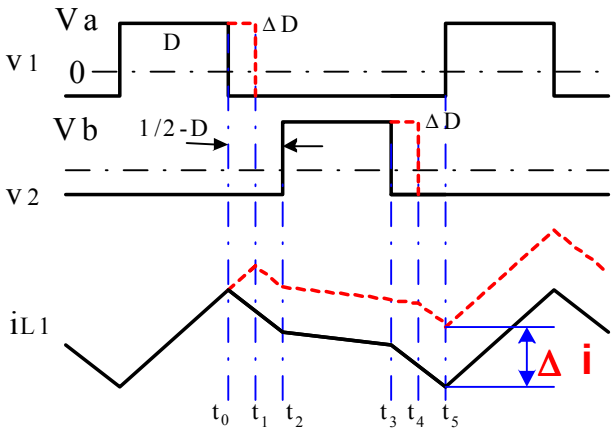

(a)

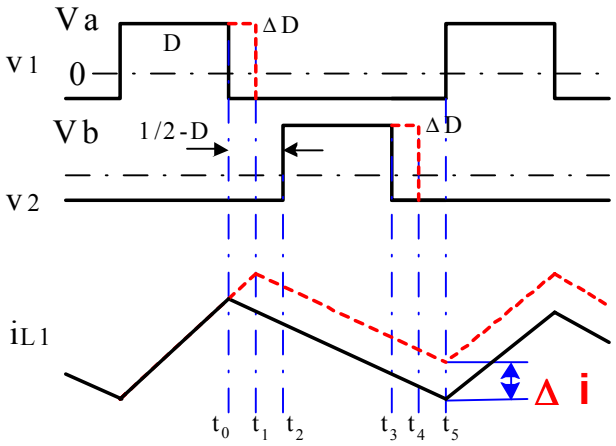

(b)

Figure 3.15. Voltage and current waveforms during the load transient: (a) the coupling case, and (b) the non-coupling case.

During the transient response, assume the duty cycle has an increase of ΔD. The steady-state inductor current waveform is the solid line. The transient inductor current waveform is the dotted line. After a switching cycle, the inductor current has an increase of Δi.

From the waveform shown for the coupling case in Figure 3.15(a), Δi can be derived as follows:

$$\Delta i_{CP} = \frac{Vs \cdot \Delta D}{(L - M) \cdot Fs} = \frac{Vs \cdot \Delta D}{Leq2 \cdot Fs}. \tag{3.24}$$

From the waveform for the non-coupling case shown in Figure 3.15(b), Δi can be derived as follows:

$$\Delta i_{NC} = \frac{Vs \cdot \Delta D}{L \cdot Fs}. \tag{3.25}$$

Comparing Equations 3.24 and 3.25, the only difference is the inductance value. To improve the transient responses, a small inductance is preferred. According to the definition of Leq2 in Equation 3.22, the coupled inductors give a smaller transient equivalent inductance. The equivalent inductance Leq2 is defined as the transient equivalent inductance.

Figure 3.16 shows the steady-state inductor voltage and current waveforms for the non-coupling and coupling cases. The inductor voltage waveforms for both cases are the

same. For the inductor current waveforms, the solid lines correspond to the coupling case, while the dashed lines correspond to the non-coupling case.

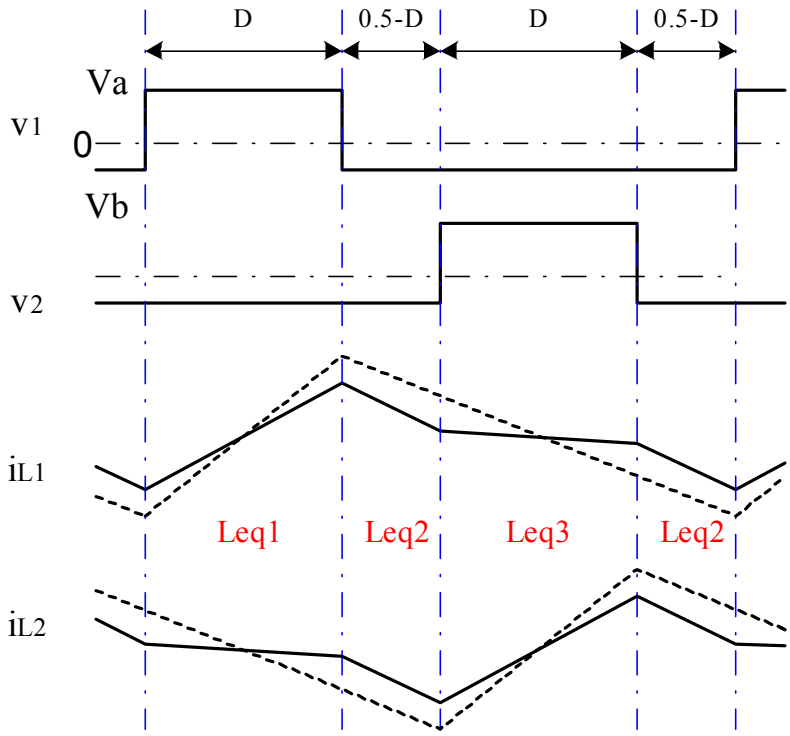

Figure 3.16. Steady-state voltage and current waveforms for the coupling case (solid lines) and the non-coupling case (dashed lines).

As shown in Figure 3.16, the steady-state inductor peak-to-peak current for the coupling case is derived as follows:

$$I_{PP\_CP} = \frac{Va \cdot D}{Leq1 \cdot Fs}. \tag{3.26}$$

As shown in Figure 3.16, the steady-state inductor peak-to-peak current for the non-coupling case is derived as follows:

$$I_{PP\_NC} = \frac{Va \cdot D}{L \cdot Fs}. \tag{3.27}$$

Comparing Equations 3.26 and 3.27, the only difference is the inductance value. For steady-state operation, a large inductance is preferred so that the current ripples can be reduced. According to the definition of Leq1 in Equation 3.21, the steady-state current ripple of the coupling case can be reduced below that of the non-coupling case. The equivalent inductance Leq1 is defined as the transient equivalent inductance.

One of major objectives of using multiphase technology is to reduce the overall output current ripples. It is also important to see the effect of coupling on the output current. The inductor currents for both the coupling and non-coupling cases are determined in Equations 3.14 and 3.15, respectively. The output current that is the sum of the inductor currents can be found by adding Equations 3.13 and 3.14. Equation 3.28 gives the output current for the coupling case, and Equation 3.29 gives the output current for the non-coupling case.

$$v_1 + v_2 = (L + M) \cdot \frac{d(i_{L1} + i_{L2})}{dt} = Leq2 \cdot \frac{di_O}{dt}, \text{ and} \tag{3.28}$$

$$v_1 + v_2 = L \cdot \frac{d(i_{L1} + i_{L2})}{dt} = L \cdot \frac{di_O}{dt}. \tag{3.29}$$

Comparing Equations 3.28 and 3.29, if the transient equivalent inductances are equal, then the output current waveforms are the same for both the coupling and non-coupling cases.

In summary, inverse coupling between the two inductors produces a smaller transient equivalent inductance (Leq2) and a larger steady-state equivalent inductance (Leq1). The inversely coupled inductors are able to improve both the transient and steady-state performances over those of non-coupling inductors.

3.3.3. Demonstration of Proposed Integrated Magnetics for 12V VRM

A 12V-input, 1.5V/50A-output VRM prototype was built using the four-phase coupled-buck converter, as shown in Figure 3.17.

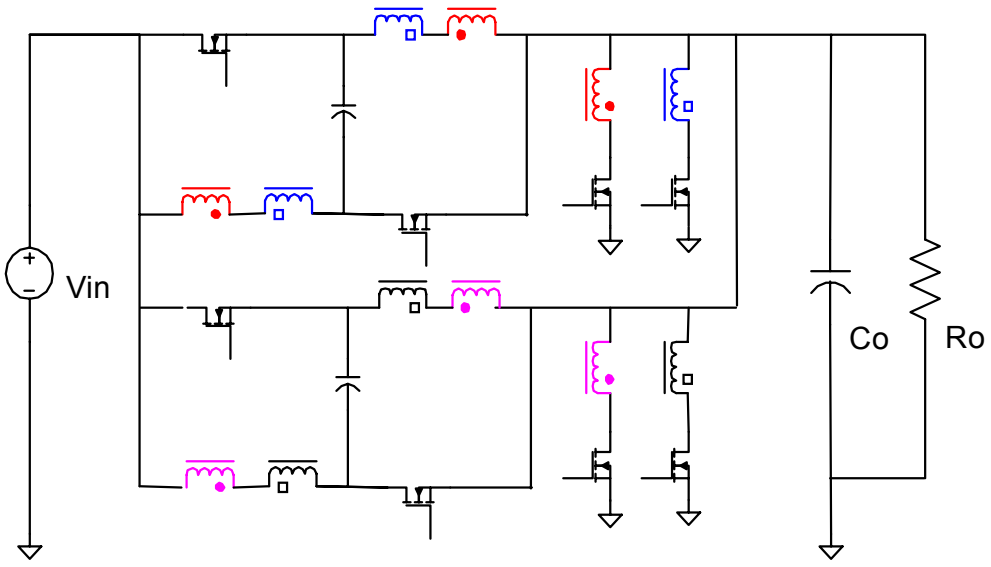

Figure 3.17. Schematic of four-phase coupled-buck converter.

The prototype operates at 300 kHz. The following components were selected for the power stage: top switch – Si4884DY; bottom switch – Si4874DY; output inductance reflected to the bottom side – 300 nH; input capacitors – 12x22 uF, and output capacitors – 6x820 uF.

Both the existing and proposed integrated magnetic structures were tested in the developed four-phase coupled-buck VRM.

Figure 3.18 illustrates the designs for these two integrated magnetic structures. Because of the small inductance requirements of multiphase VRMs, one turn can be used for the secondary windings. PCB winding and the planar cores can be used to reduce the profile of the power stage.

The two channels with phase shifts of 0^o and 180^o share a pair of cores, while the other two channels with phase shifts of 90^o and 270^o share another pair of cores. Their magnetic cores are a pair of E18/4/10-3F3 and PLT18/10/2-3F3. The turns ratio of the coupled inductors is 2:1. Both top windings have two turns, and the bottom winding has only one turn. Two top winding are built on each side of 4oz double side PCBs. The bottom winding is made of two layers of paralleled 5mil copper foils, and each of them is placed on the top of two-turns windings.

The design of the core structures is based on the same transient equivalent inductance (about 300 nH in each channel). Assuming that the reluctances of the cores can be ignored, the air gaps for both core structures are designed as follows.

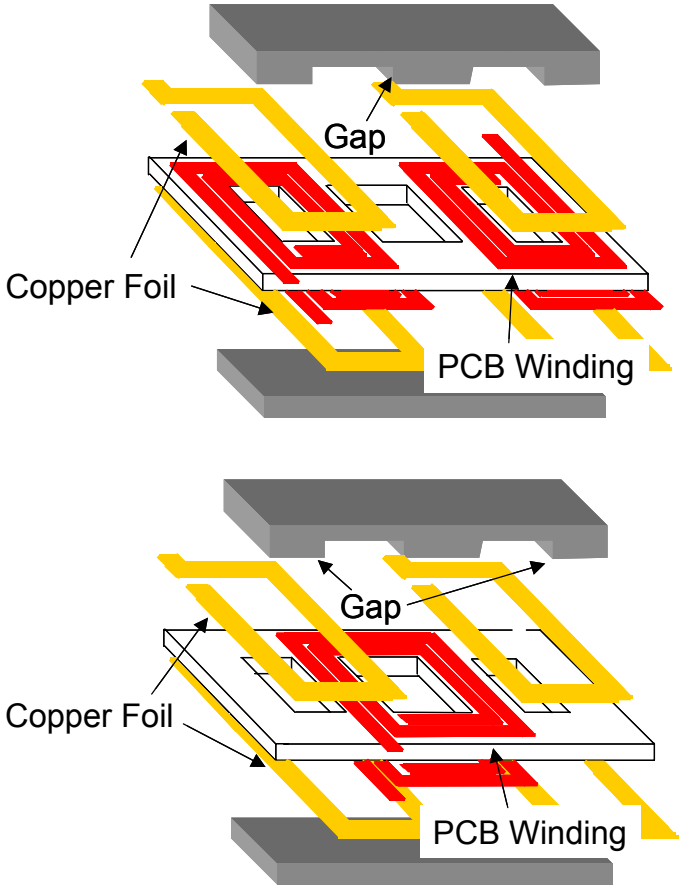

Figure 3.18. Implementation of integrated magnetics in the four-phase coupled-buck VRM: (a) proposed structure, and (b) existing structure.

For the core structure in the existing integrated magnetics, the air gap in the outer leg can be easily derived, as follows:

$$l_{G\_NC} = \mu_0 \cdot A_O \cdot \frac{N^2}{L_{NC}}, \tag{3.30}$$

where A_O is the cross-section area of the outer leg, and l_{G_NC} is the air gap in the outer leg.

For the core structure in the proposed integrated magnetics, the air gap in the center leg can be derived as follows:

$$l_{G\_CP} = \mu_0 \cdot \frac{A_C}{2} \cdot \frac{N^2}{L_{CP}}, \tag{3.31}$$

where A_C is the cross-section area of the center leg, and l_{G_CP} is the air gap in the center leg.

For the specific core used in the evaluation, the cross-section area of the center leg is twice that of the outer legs. The air gap in the center leg of the proposed integrated magnetics is the same as that in the outer legs of the existing integrated magnetics (about 6 mil).

Finite-element-analysis (FEA) simulations are conducted in order to quantify the core losses and winding losses in both the existing and the proposed integrated magnetics. The fundamental component of the winding currents is used. The frequency of the sinusoidal waves in the simulation is 300 kHz.

Figure 3.19 shows the FEA results of the AC flux distribution in the core structures of the existing and proposed integrated magnetics. As discussed previously, in the existing structure, the AC fluxes are added in the center leg, while in the proposed structure, the AC fluxes are cancelled in the center leg. With the AC flux cancellation in the center leg, the proposed integrated magnetic structure has a lower core loss in the center leg.

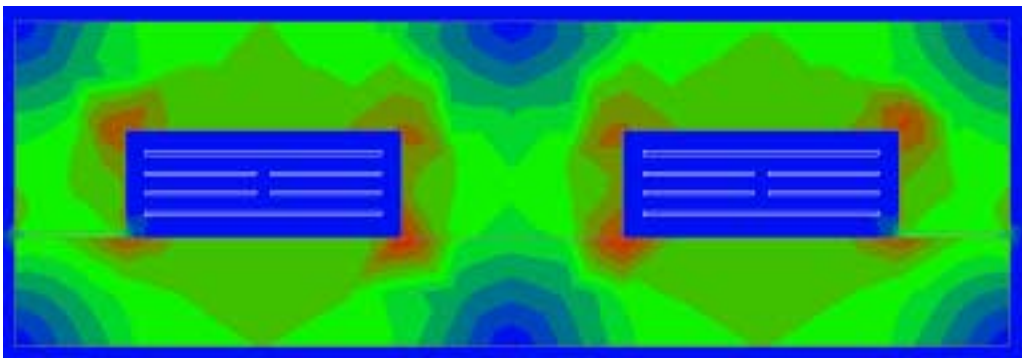

(a)

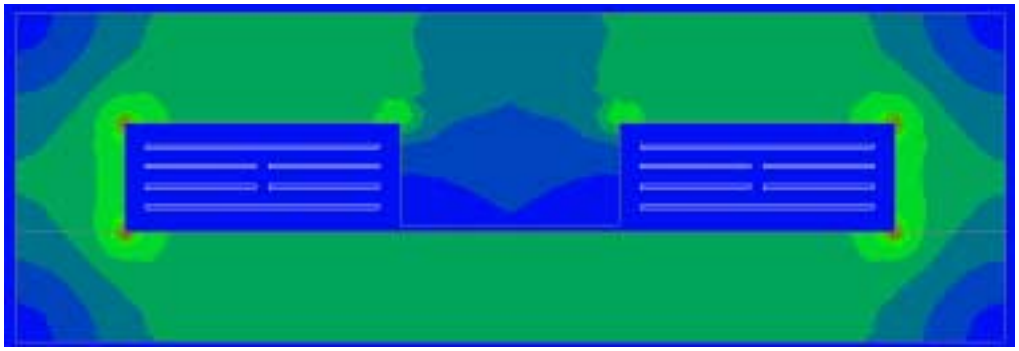

(b)

Figure 3.19. AC flux distributions: (a) in the existing structure, and (b) in the proposed structure.

The first-order approximation is used for the core loss estimation. Figure 3.20 shows the percentage of core loss reduction in the center leg. Compared with the existing structure, the proposed structure can reduce the core loss by more than 90% in the center leg.

Another advantage of the AC flux cancellation in the center leg is the much smaller fringing effects and fewer EMI problems caused by the air gap. The eddy currents in the windings cause additional winding conduction losses, which are indicative of the fringing

effects of the cores. Figure 3.21 shows the FEA results of the current distribution in the windings of the existing and proposed structures.

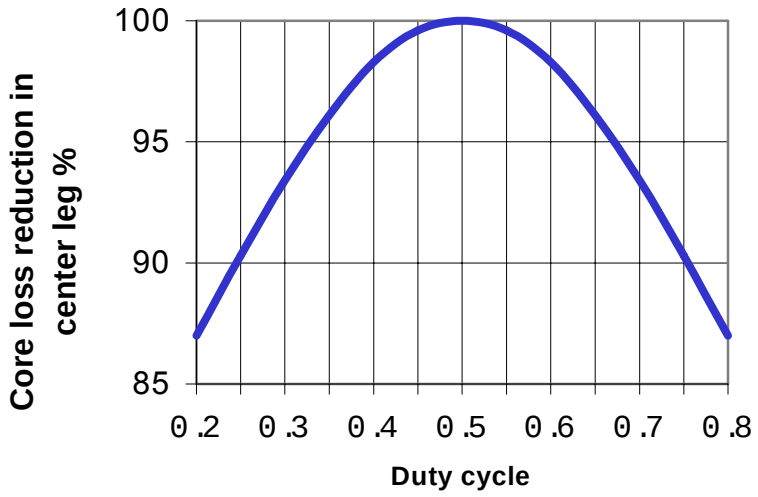

Figure 3.20. Core loss reduction in the center leg of proposed structure.

Large air gaps are usually associated with fringing effects and EMI problems. However, in the proposed structure, the AC flux through the air gap in the center leg is much smaller. Therefore, the fringing effects associated with the center leg air gap are much smaller. The fewer the eddy currents generated in the windings, the lower the winding loss will be. Figure 3.22 shows the winding losses for both the existing and the proposed integrated magnetics.

As can be seen from Figure 3.22, the proposed structure can offer about 75% lower winding AC loss than the existing structure.

As discussed previously, the two output inductors in the proposed structure are coupled with a coupling coefficient close to one while the two inductors in the existing structure are decoupled. The steady-state current ripple of the coupling case is expected to be smaller than that of the non-coupling case. Correspondingly, the semiconductor devices have smaller current ripples and RMS currents.

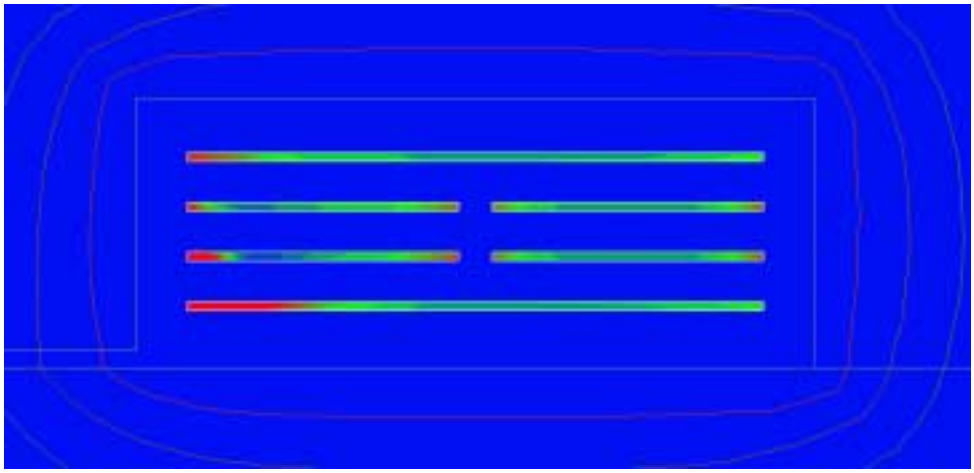

(a)

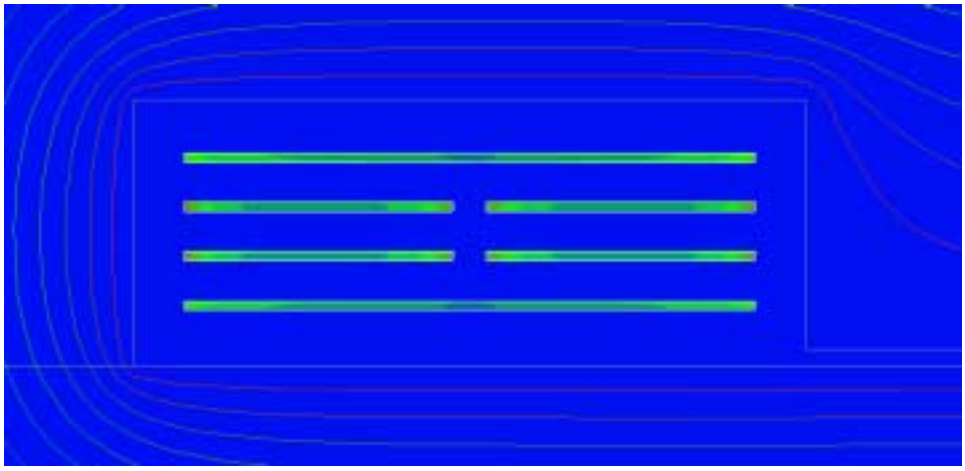

(b)

Figure 3.21. Winding current distributions: (a) in the existing structure, and (b) in the proposed structure.

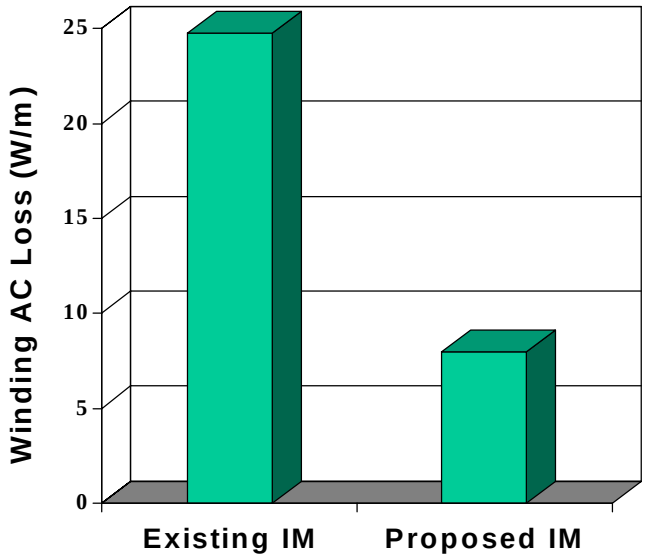

Figure 3.22. Winding loss reduction in the proposed integrated magnetic structure.

Figure 3.23 shows the current waveforms in both the primary and secondary switches. With the proposed integrated magnetics, the primary switches can offer a lower RMS current and a lower current ripple, and the secondary switches can offer a lower RMS current. Correspondingly, the proposed structure can offer lower switching and conduction losses that the existing structure.

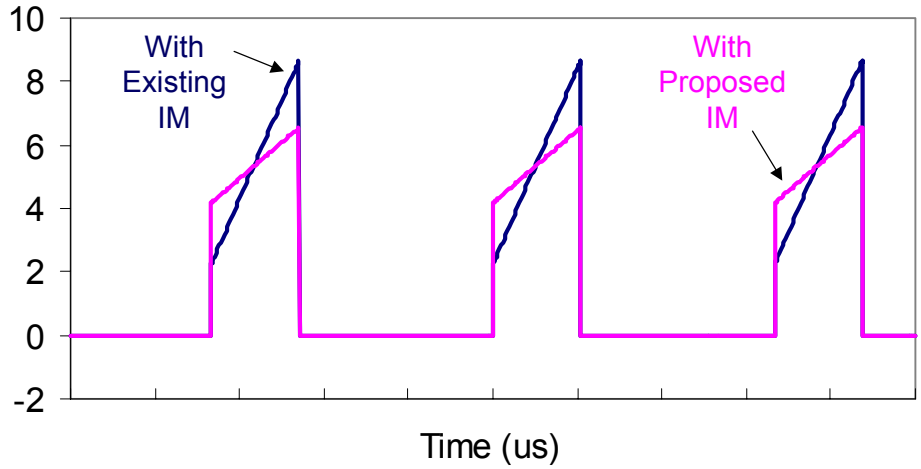

(a)

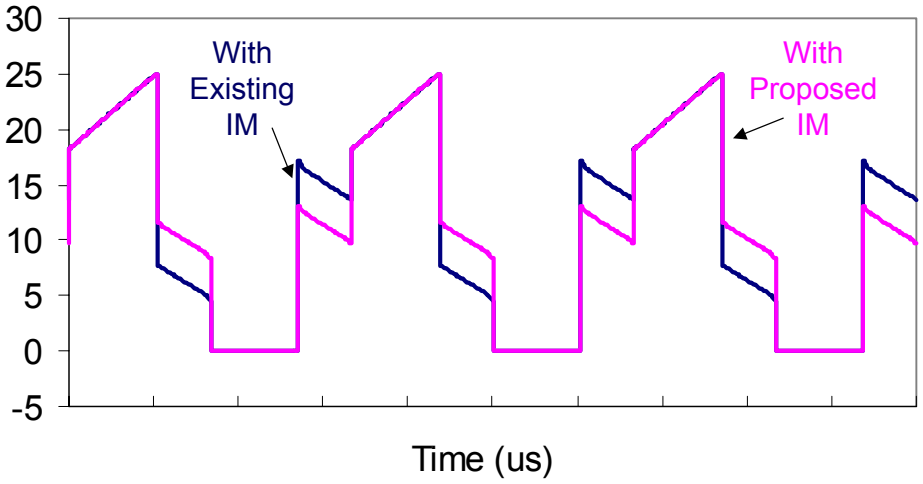

(b)

Figure 3.23. Current waveforms: (a) in primary switches, and (b) in secondary switches.

In summary, the proposed structure can offer a lower core loss, a lower winding loss, and lower switching and conduction losses than the existing structure. The resulting VRM is expected to have a high efficiency.

Figure 3.24 shows the power stage measured efficiency of the four-phase coupled-buck VRM with the existing and proposed integrated magnetic structures.

As can be seen from Figure 3.24, compared to the existing structure, the proposed integrated magnetic structure can offer a 2.5% improvement in efficiency at full load, and 3~4% improvement in efficiency at the ceiling point.

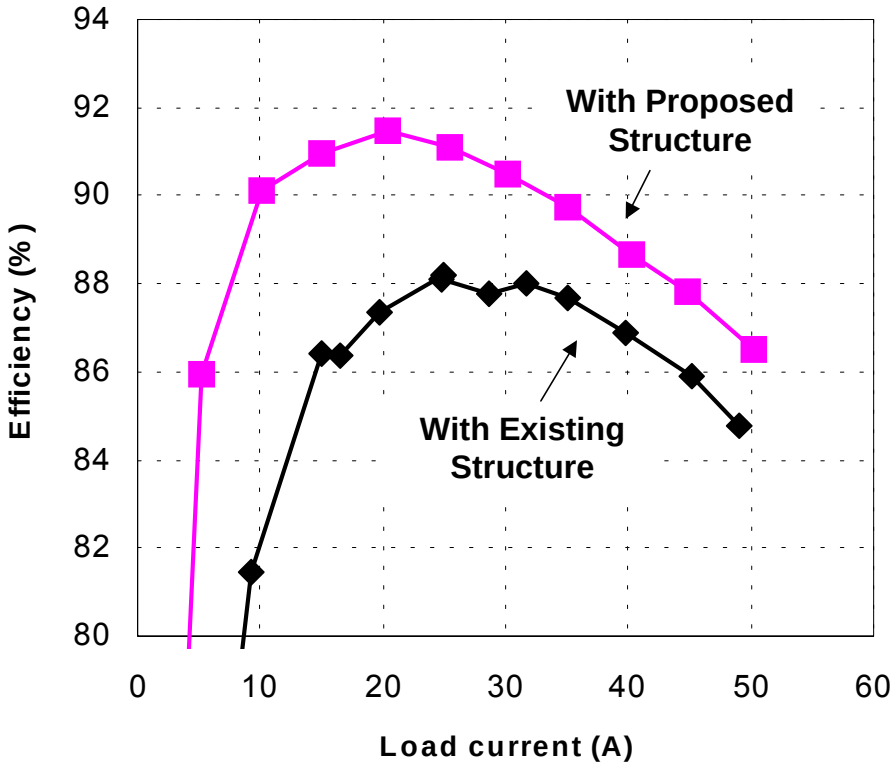

Figure 3.24. Measured power-stage efficiency of four-phase coupled-buck VRM with existing and proposed integrated magnetic structures.

3.3.4. Demonstration of Proposed Integrated Magnetics for 48V VRM

Both the existing and the proposed integrated magnetic structures were tested in a push-pull forward VRM at V_{IN} = 48 V, V_O = 1.2 V, I_O = 70 A, and F_S = 100 kHz.

Figure 3.25 illustrates the designs for these two integrated magnetic structures. Their magnetic cores are a pair of E32-3F3 and PLT32-3F3. Their windings are made in eight-layer 2oz PCBs; four layers for the two primary windings and four layers for the

secondary winding. Each of the two primary windings has eight turns with four turns per layer. The secondary winding has one turn with four layers paralleled.

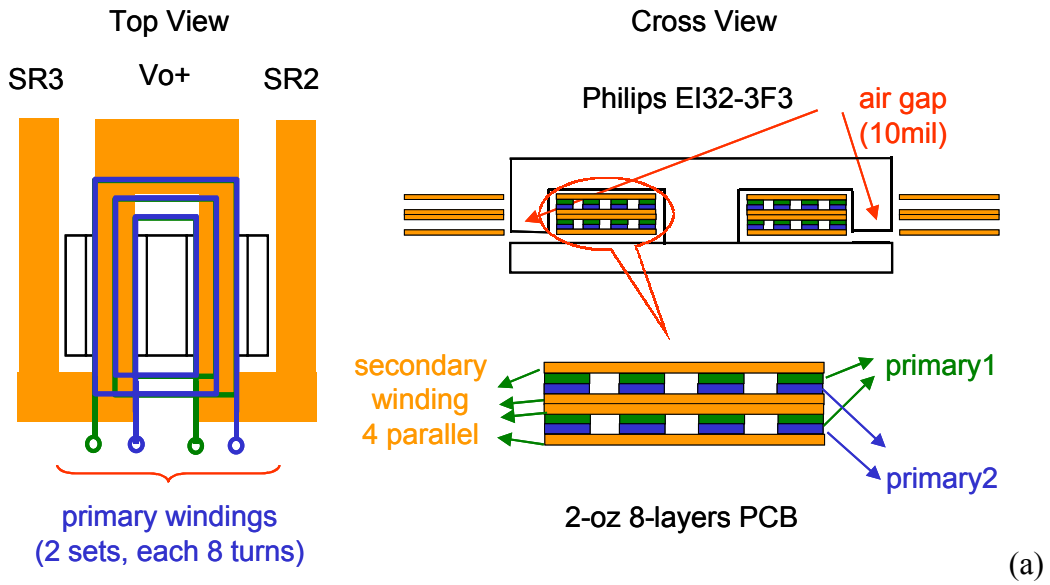

(a)

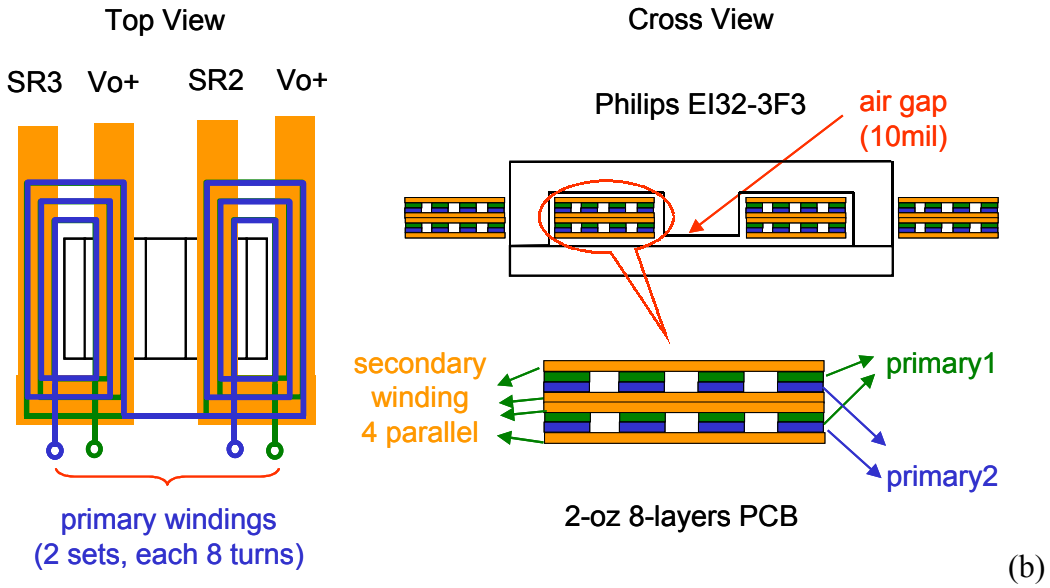

(b)

Figure 3.25. Integrated magnetic designs: (a) existing structure, and (b) proposed structure.

In order to provide a meaningful efficiency comparison, the inductor values are designed to meet the same transient response. As discussed in the preceding section, air gaps of equal lengths can achieve equal transient equivalent inductances. In the existing structure, each of the outer legs has a 10mil air gap and there is no air gap in the center leg. In the proposed structure, only the center leg has a 10mil air gap.

Figure 3.26 shows the FEA results of the AC flux distribution in the core structures of the existing and proposed integrated magnetics. As discussed previously, in the existing structure, the AC fluxes are added in the center leg, while in the proposed structure, the AC fluxes are cancelled in the center leg. With the AC flux cancellation in the center leg, the proposed integrated magnetic structure has a lower core loss in the center leg.

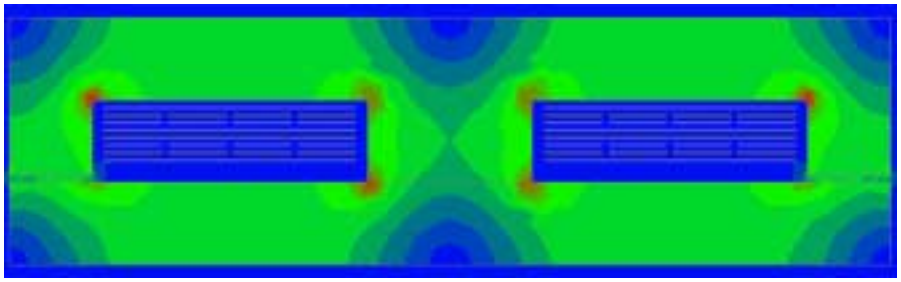
(a)

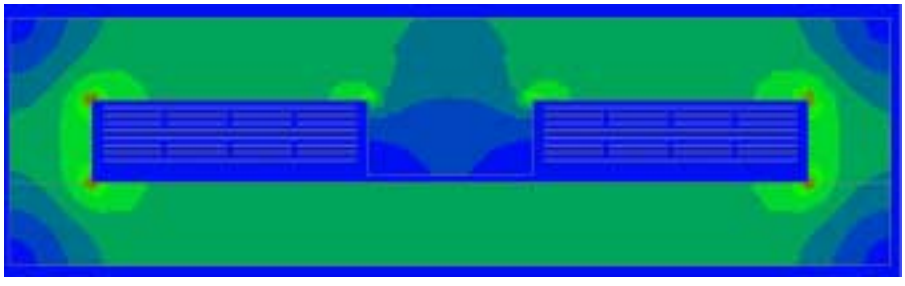
(b)

Figure 3.26. AC flux distributions: (a) in the existing structure, and (b) in the proposed structure.

As with the 12V VRM, another advantage of the AC flux cancellation in the center leg is the much smaller fringing effects and fewer EMI problems caused by the air gap. The AC flux through the air gap in the center leg is much smaller than in the outer legs. The fringing effects associated with the center leg air gap are also much smaller. The fewer the eddy currents generated in the windings, the lower the resulting winding loss will be. Maxwell two-dimensional (2D) field simulator provides the current distribution in the windings. The winding current distributions from FEA are shown in Figure 3.27.

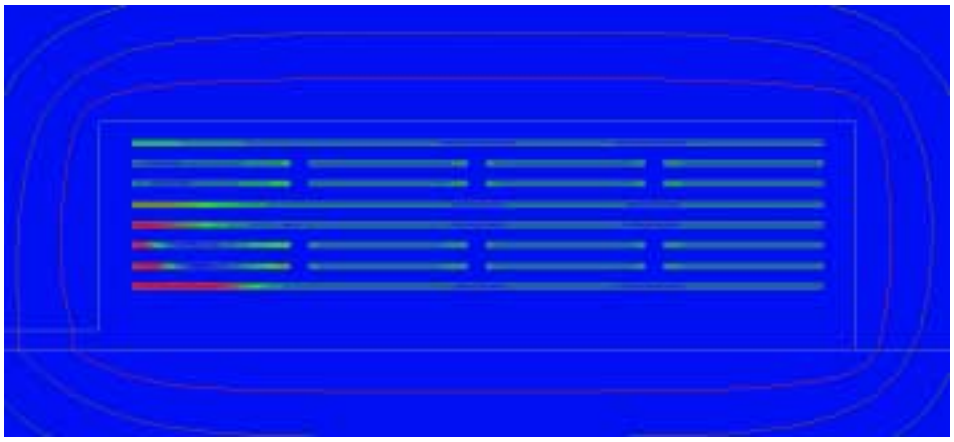

(a)

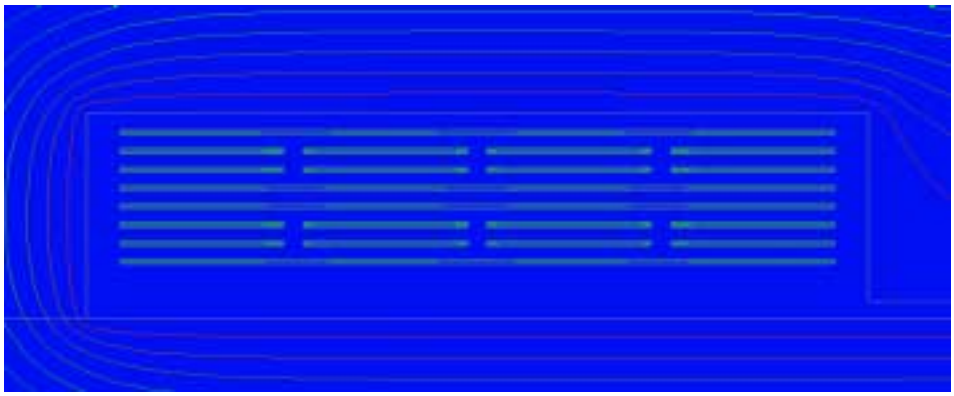

(b)

Figure 3.27. Winding current distributions: (a) in the existing structure, and (b) in the proposed structure.

The measured leakage inductances at the secondary side are 15 nH in the proposed structure and 60 nH in the existing structure. The proposed structure can reduce the leakage inductance by three times that of the existing structure. Figure 3.28 shows the experimental waveforms with these two structures at I_O = 70 A.

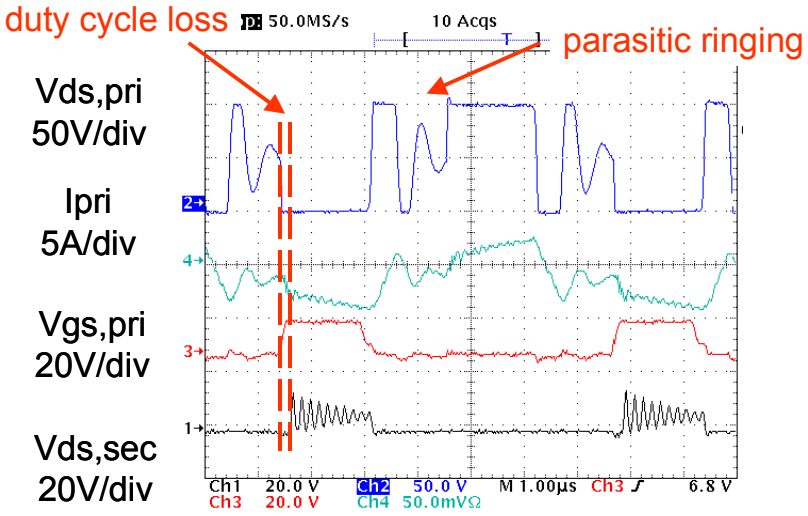

(a)

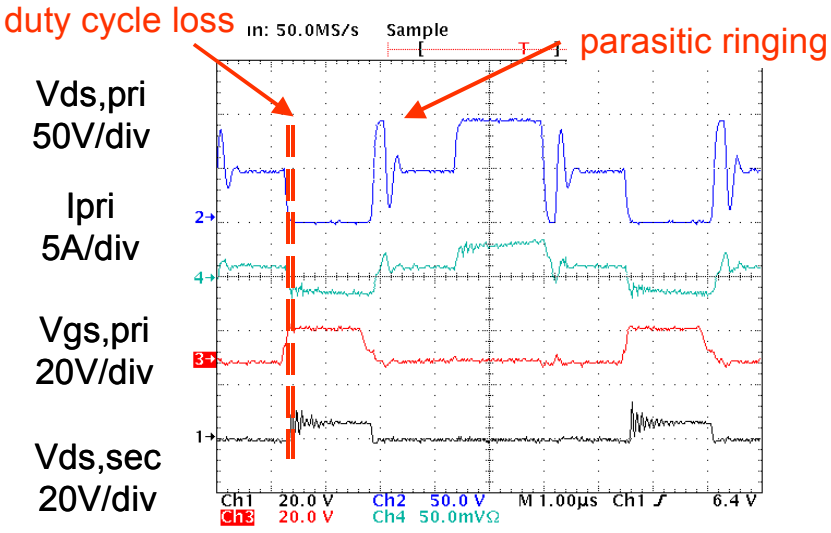

(b)

Figure 3.28. Experimental waveforms at full load: (a) with the existing structure, and (b) with the proposed structure.

As can be seen from Figure 3.28, the proposed structure offers less parasitic ringing, a lower current ripple and a smaller duty cycle loss at the secondary side than the existing structure.

Figure 3.29 shows the power-stage efficiency with these two structures. Compared to the existing structure, the proposed structure can offer a 3% improvement in efficiency.

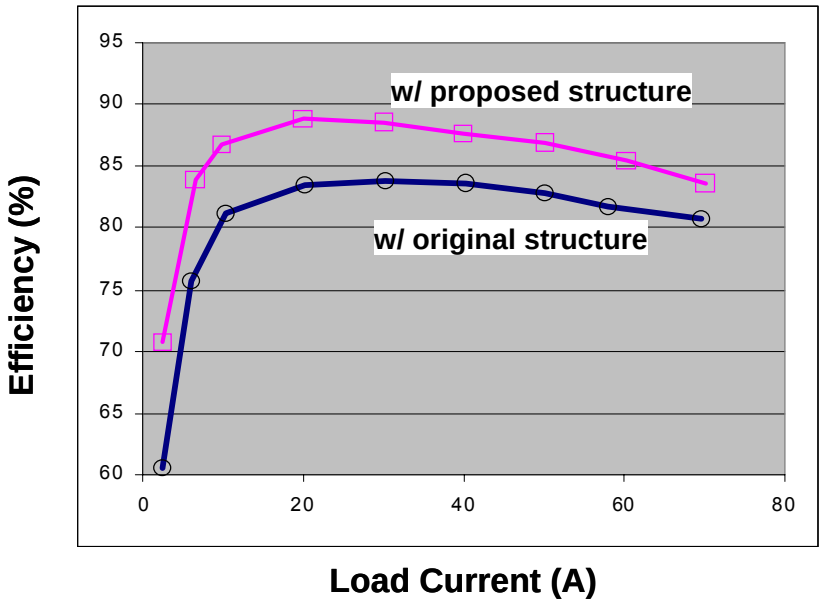

Figure 3.29. Measured power-stage efficiency for 48V VRM.

3.4. INTEGRATION OF INPUT FILTER INTO PROPOSED IM STRUCTURE

The preceding magnetic integration approach only combines the transformer with output filter inductors. The issue of further integration of the input filter inductor is

addressed in this section. With the proposed structure, it is possible to use only a single magnetic core for the entire converter.

3.4.1. Concept of Built-in Filter

Because of the inductor coupling, the output current of the multiphase coupled-buck converter pulses. As a result, the RMS current through the output capacitors is increased, and consequently, the output ripple voltage is also increased. This pulsing output current also increases the switching noise of the output voltage because of the presence of the effective series inductance (ESL) in the output capacitor. In order to smooth the pulsing input and output currents, two additional L-C filters are required, as shown in Figure 3.30.

To solve the problems associated with the pulsing output current, an improved multiphase coupled-buck converter is proposed, as shown in Figure 3.31.

The operation principle of the improved multiphase coupled-buck converter is the same as that of the original one as described in Section 2.3. Figure 3.32 shows its key operation waveforms. Compared to the original multiphase coupled-buck converter, the improved multiphase coupled-buck converter has smooth input and output currents.

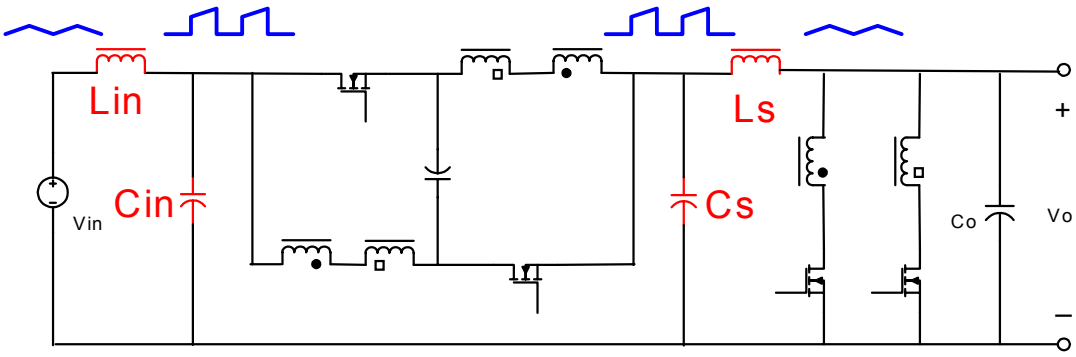

Figure 3.30. Pulsing input and output currents of multiphase coupled-buck converter require additional L-C filters.

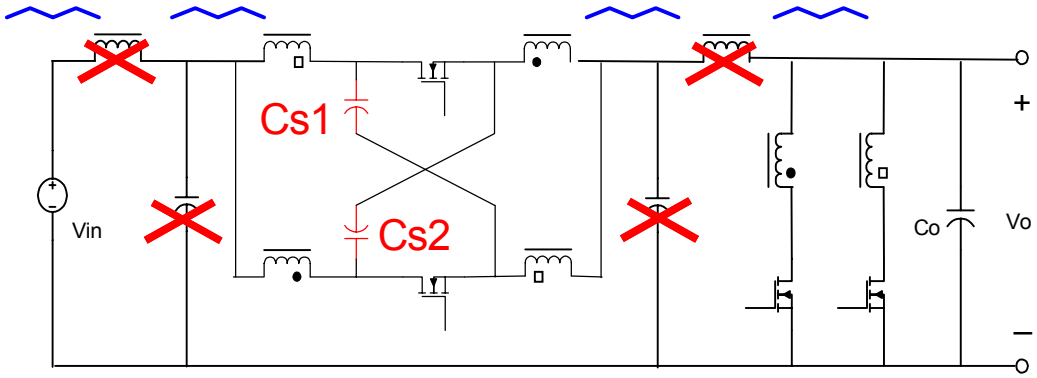

Figure 3.31. Improved multiphase coupled-buck converter features built-in filters.

The integration of built-in input and output filters in the improved multiphase coupled-buck converter can be explained by Figure 3.33. Starting from the original multiphase coupled-buck converter with additional L-C filters, the filtering and clamping capacitors Cin, Ca and Cc are shifted to a new location without changing the filtering and clamping functions, as shown in Figure 3.33(b). Next, the filtering inductors Lin and La are shifted to positions in series with the inductor windings. The resulting topology is the

improved multiphase coupled-buck converter, where the leakage inductances of coupled output inductors are shown.

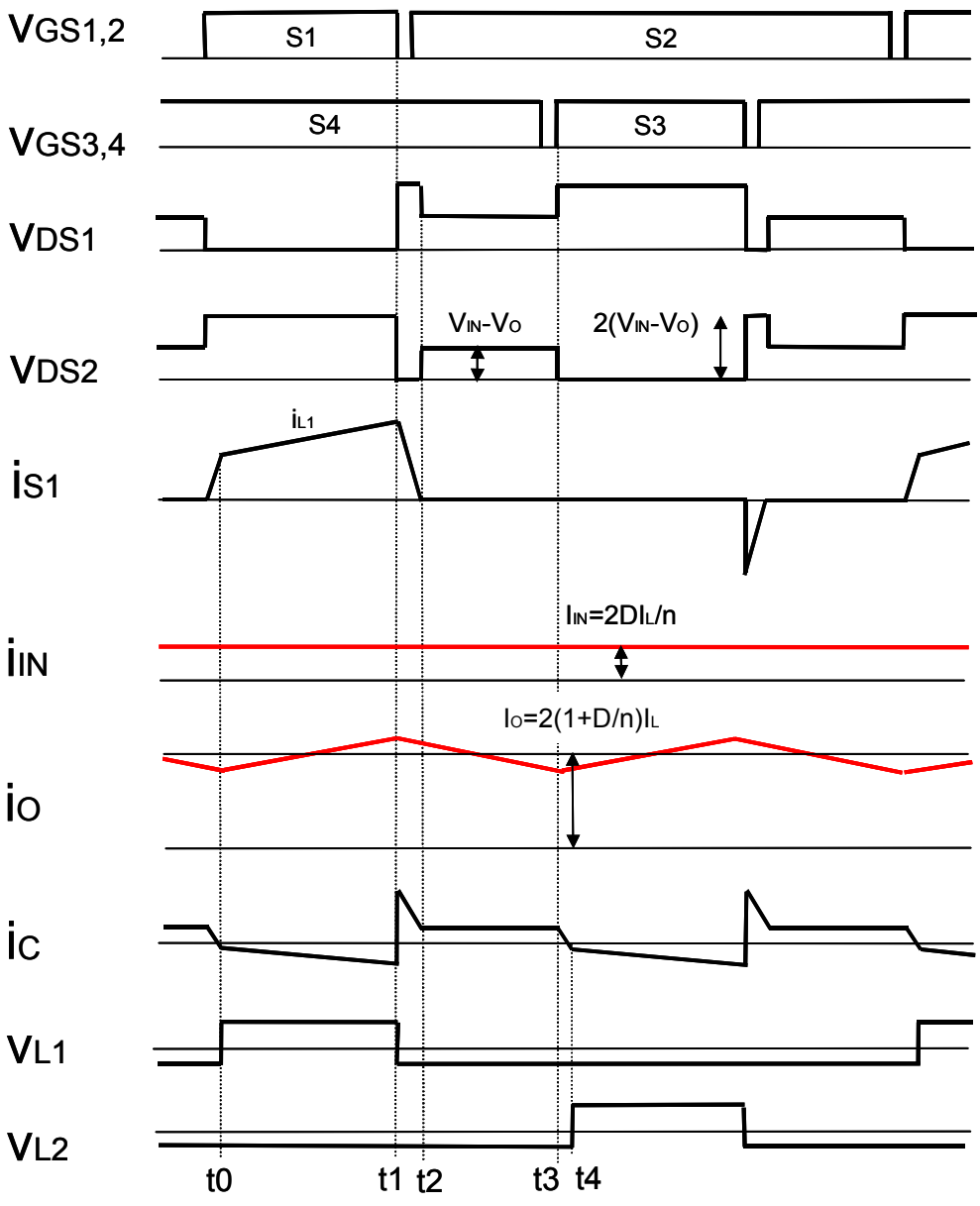

Figure 3.32. Key operation waveforms of the improved multiphase coupled-buck converter.

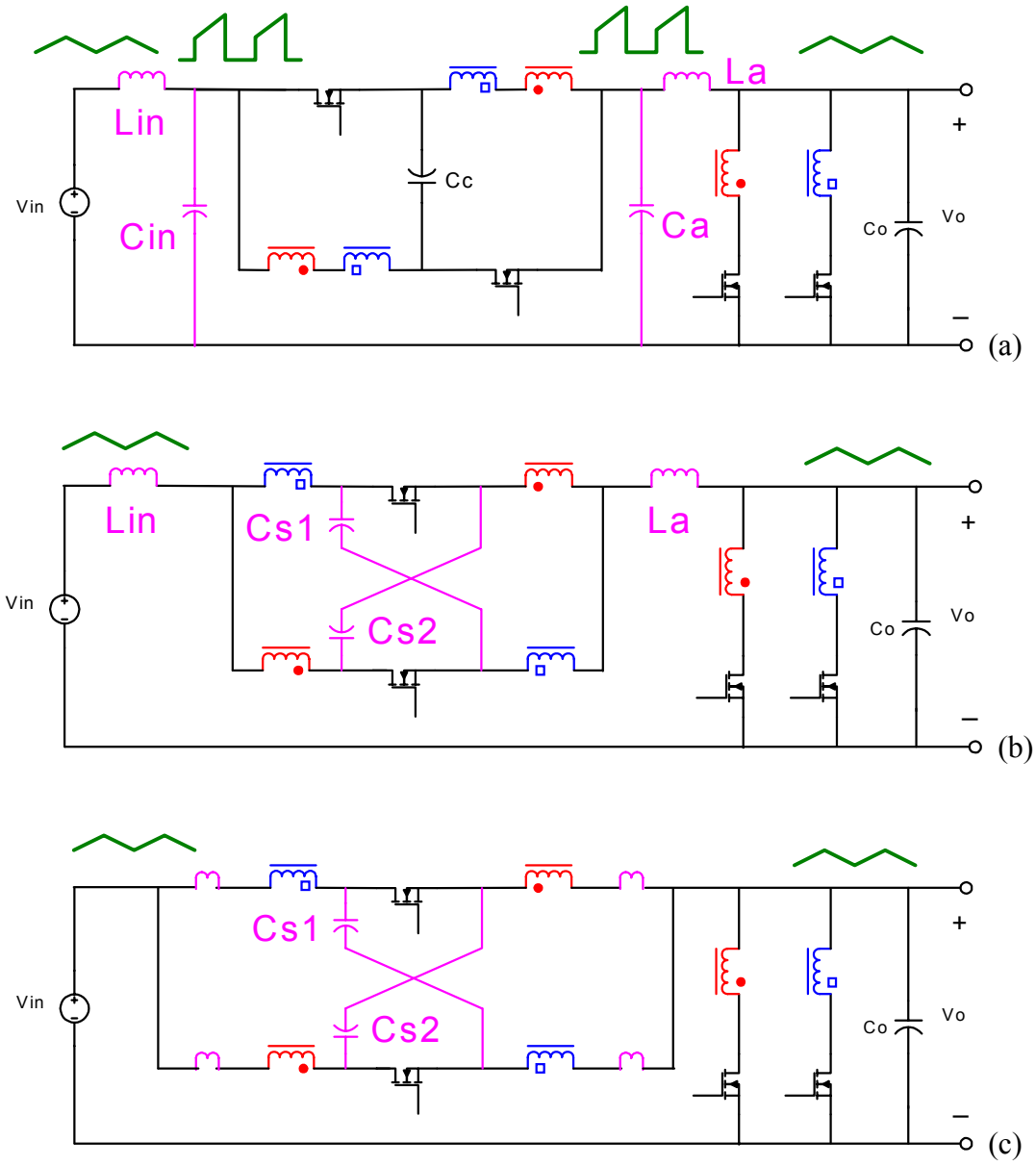

Figure 3.33. Integration of L-C filters in multiphase coupled buck converter: (a) with additional L-C filters, (b) capacitor shifting, and (c) inductor shifting.

Based on the preceding manipulations, in improved multiphase coupled-buck converter the built-in filters are formed by the leakage inductance and the clamping

capacitors C_{S1} and C_{S2}. The same concept of built-in filters has also been used for other applications.

It's interesting to notice that the improved multiphase coupled buck converter can be viewed as the simplification of the multiphase tapped-inductor buck converter.

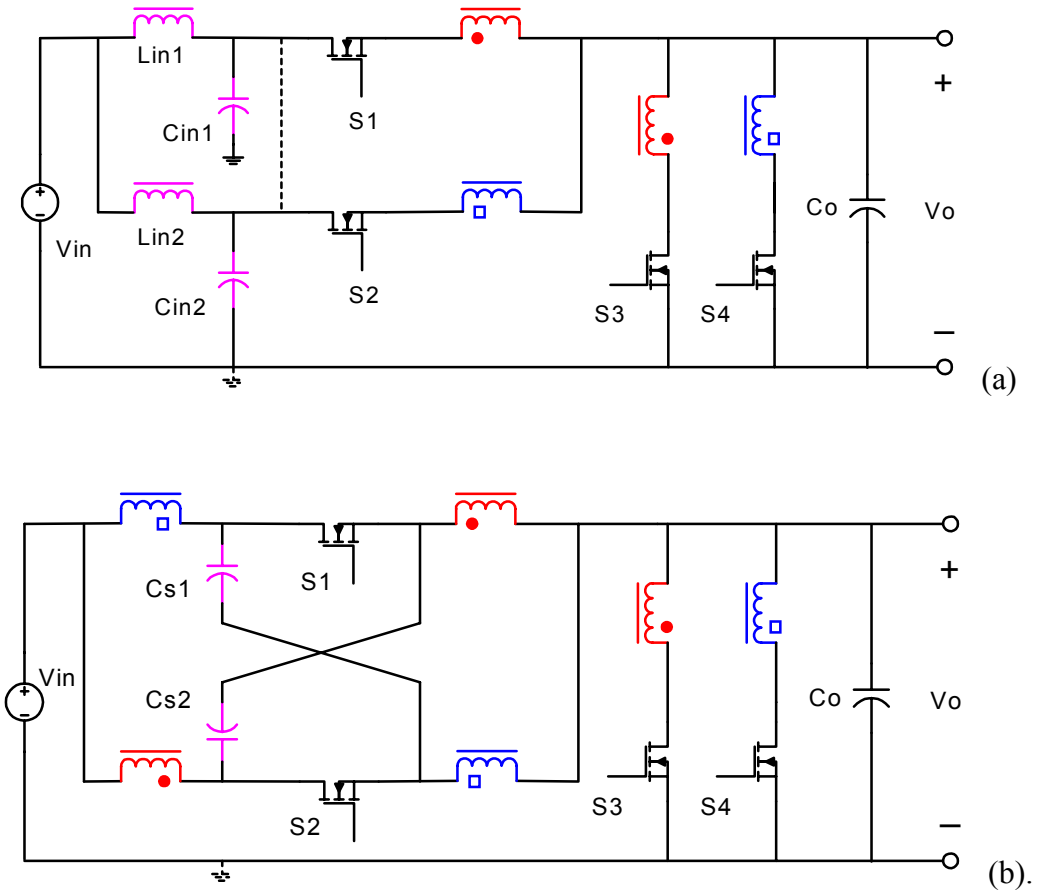

Figure 3.34. Derivation of improved coupled buck converter: (a) multiphase tapped-inductor buck converter with external L-C filters, and (b) multiphase coupled buck converter with built-in filters.

As shown in Figure 3.34, by coupling the input filter inductors with the output inductors in the neighboring channels, and at the same time shifting the input capacitors to the places where the capacitor voltages remain constant, the improved multiphase coupled-buck converter is derived from the multiphase tapped-inductor buck converter.

3.4.2. Design of Built-in Filters

Due to the existence of the built-in input filter in the improved multiphase coupled-buck converter, the input filter size can be reduced, and sometimes no external input filter is needed. As shown in Figure 3.35, there are two ways to implement the input filter for the improved multiphase coupled-buck converter.

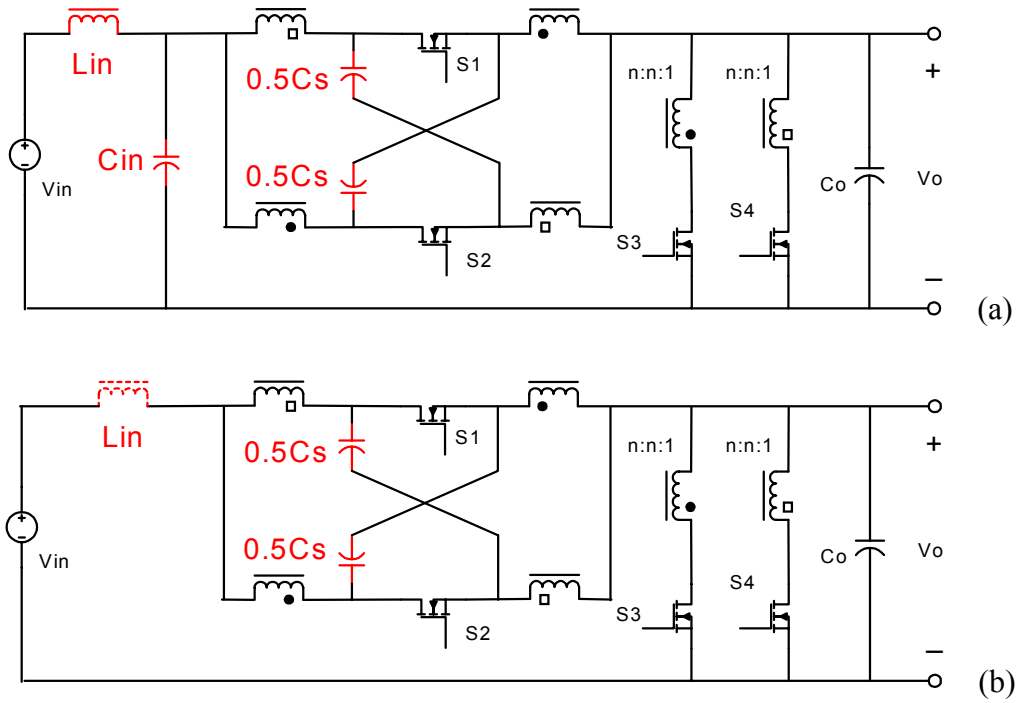

Figure 3.35. Two implementations for the input filter in the multiphase coupled-buck converter: (a) with external filter, and (b) with fully integrated filter.

In Figure 3.35(a), the external filter inductor and capacitor are used and the clamping capacitor is designed according to the clamping requirement. In Figure 3.31(b), no external input capacitor is used and the clamping capacitor is designed according to the input filter requirement. Depending on the value of the leakage inductance, the external inductor may not be needed in the structure shown in Figure 3.35(b).

Since various applications may have different design criteria for the input filter, in order to see the influence of the built-in filter on the input filter design, 12V VRMs are used as the example in the following discussion.

For 12V VRMs, the major concern on the input filter design is the input current slew rate during the load transients. According to the Intel VRM 9.0, the input current slew rate should not exceed 1 A/us at the worst load transient conditions.

Figure 3.36 shows the simplified circuit model for the VRM input filter design. As shown in Figure 3.36, the difference between the two current waveforms causes the unbalanced charges that need to be provided by the corresponding capacitors. The unbalanced charges can be approximated as the shaded areas shown in Figure 3.36. The definitions of the currents and unbalanced charges are in given in Figure 3.36. Based on the unbalanced charges, the input capacitance can be estimated as follows:

$$C_{IN} > \frac{I_{IN}}{2 \cdot \Delta V_{IN}} \cdot \left(\frac{I_{IN}}{di_{IN}/dt} - \frac{I_{IN}}{di_{K}/dt} \right), \tag{3.32}$$

where $\frac{di_K}{dt} \approx \frac{2}{\pi} \cdot \frac{I_{IN}}{\sqrt{L_K \cdot C_S}}$ is the input current slew rate after the built-in input filter if Figure 3.35(a)'s external input filter is used, otherwise, $\frac{di_K}{dt} = \frac{di_S}{dt}$ is the output inductor slew rate. I_{IN} and ΔV_{IN} are the input average current and maximum input voltage overshoot during transients, respectively.

The preceding formula gives the minimum requirement of the VRM input capacitance. Of course, the ESR and ESL of the capacitors also influence the input filter design, but these will not be discussed further.

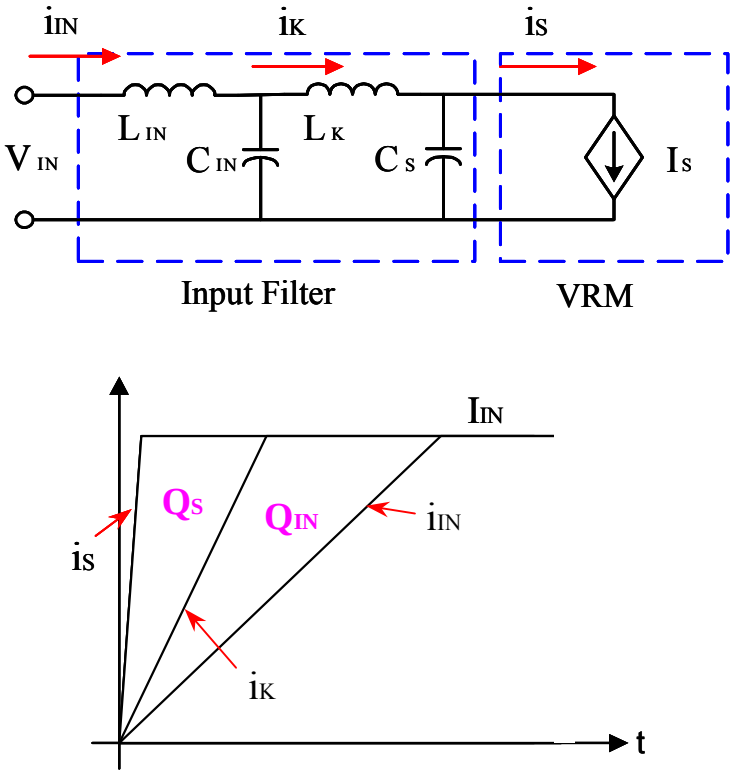

Figure 3.36. Simplified circuit model for the VRM input filter design.

The input inductor limits the input current slew rate under the requirement. After the input capacitance is chosen, the input inductance can be estimated as follows:

$$L_{IN} > \frac{1}{C_{IN}} \cdot \left(\frac{2}{\pi} \cdot \frac{I_{IN}}{di_{IN}/dt} \right)^2 . \tag{3.33}$$

Table 3.1 summarizes the design parameters for the two input filter implementations shown in Figure 3.35. As a comparison, it also includes the case without the built-in filter. They are designed according to the following specifications: V_{IN}=12 V, V_O=1.5 V, and I_O=50 A.

Table 3.1. Input filter designs: (Case I has no built-in filter, only an external filter; Case II has both a built-in and an external filter; and Case III has a fully integrated filter).

	Lin	Cin	Lk	Cs
Case III	0	0	0.18uF	120uF
Case II	0.08uH	80uF	0.12uH	20uF
Case I	0.18uH	120uF	0	0

As can be seen from Table 3.1, the existence of the built-in filter reduces the input inductance by 55% and the input capacitance by 30%. The input filter can be fully integrated with the clamping circuit by controlling the leakage inductance.

3.4.3. 12V VRM with Built-in Filter and Experimental Results

A 12V-input, 1.5V/50A-output VRM prototype was built using the improved four-phase coupled-buck converter, as shown in Figure 3.37.

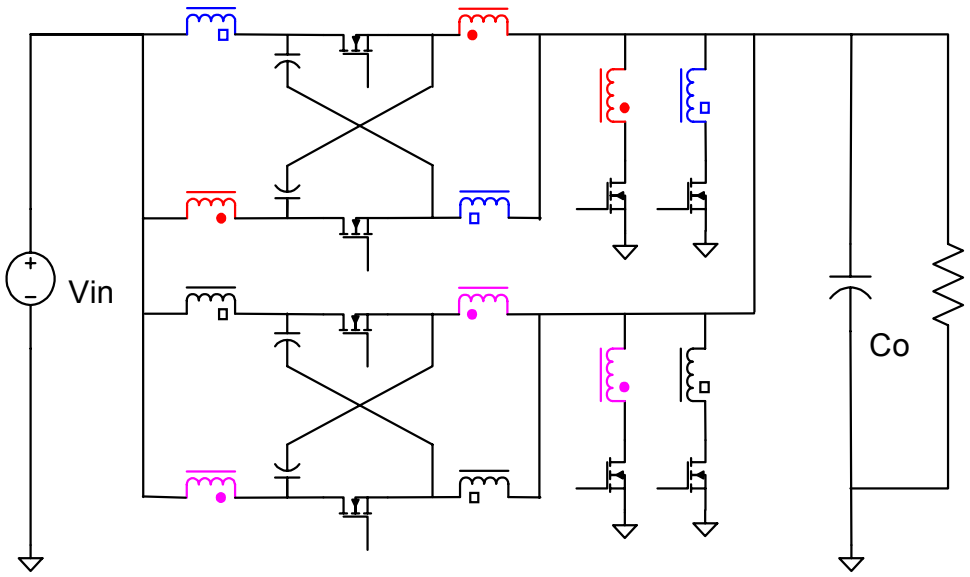

Figure 3.37. Schematic of the four-phase improved coupled-buck converter.

The prototype operates at 300 kHz. The following components were selected for the power stage: top switch – Si4884DY; bottom switch – Si4874DY; output inductance reflected to the bottom side – 300 nH; input capacitors – 12x22 uF, and output capacitors – 6x820 uF. Figure 3.38 shows the photograph of the improved four-phase coupled-buck VRM.

Figure 3.39 shows the measured waveforms at full load for the improved four-phase coupled-buck VRM. The gate drive signal for the top switch V_{GS1} is generated using the same boostrap driver as was used for the buck converter. Because of the existence of built-in filters, the input current is ripple-free in the improved multiphase coupled-buck converter, as shown in Figure 3.39.

Figure 3.38. Hardware of four-phase improved coupled-buck VRM.

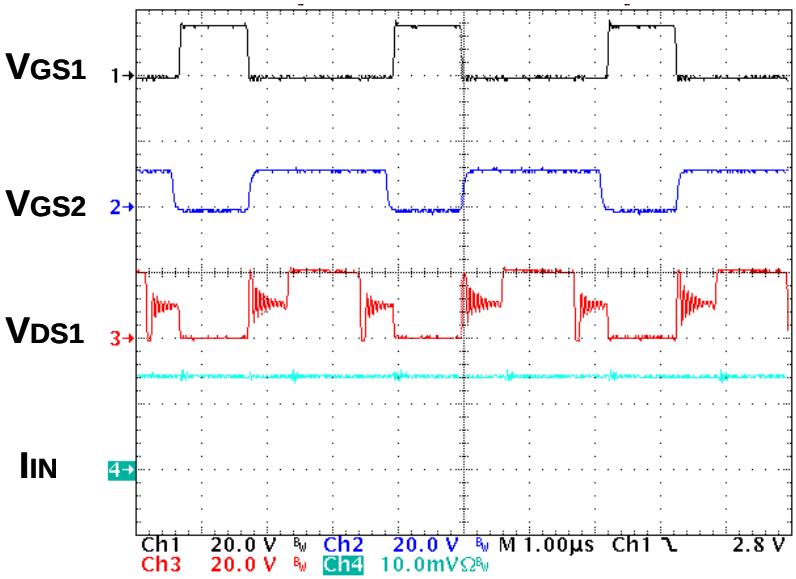

Figure 3.39. Measured waveforms of the improved coupled-buck VRM.

Figure 3.40 shows the measured power-stage efficiency of the improved four-phase coupled-buck VRM. It has a 90% ceiling efficiency and an 86% full-load efficiency.

Because of lower filter losses due to smooth input and output currents, the improved four-phase coupled-buck VRM has a 1% higher efficiency at full load than the original four-phase coupled-buck VRM, and more than 1% at light load.

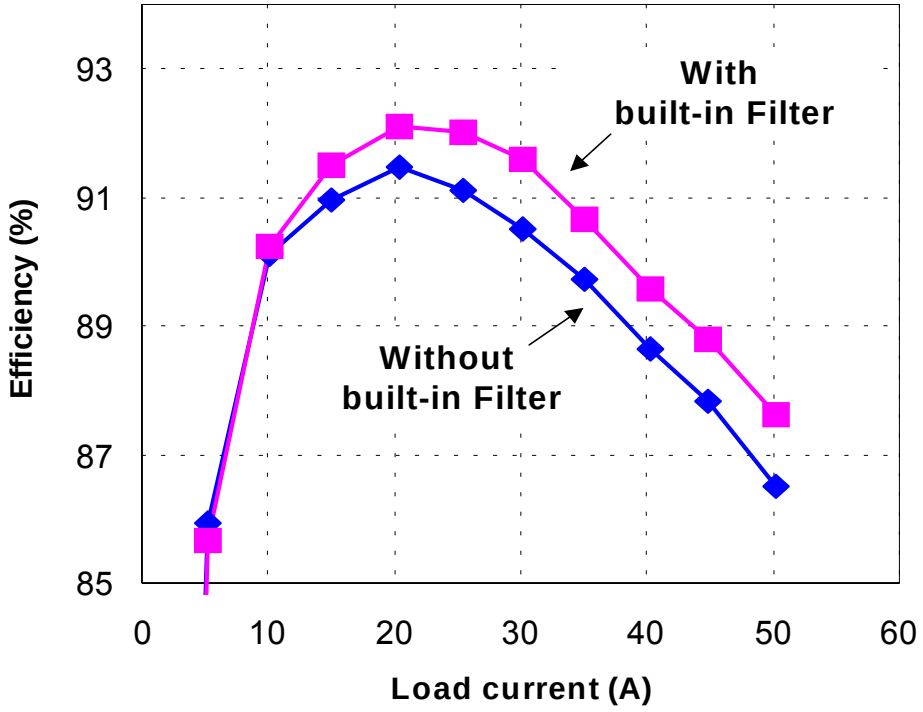

Figure 3.40. Measured efficiency of the four-phase improved coupled-buck VRM.

3.4.4. Improvement of 48V VRM with Built-in Filter

3.4.4.1. Improved Push-Pull Forward Converter with Built-in Filter

Figure 3.41 shows the push-pull forward converter with the proposed integrated magnetics for the current-doubler rectifier, and its corresponding electrical equivalent circuit for which the split transformer windings are shown.

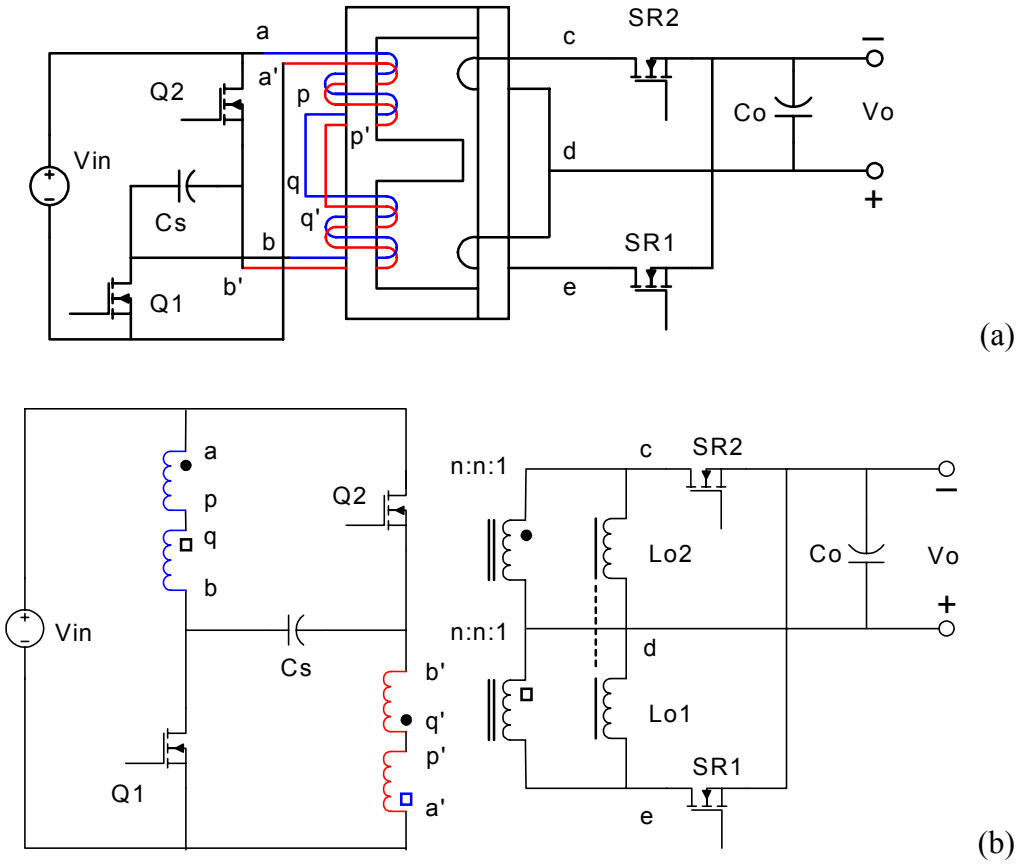

Figure 3.41. Push-pull forward converter with proposed integrated magnetic structure: (a) implementation, and (b) electrical equivalent circuit, for which the split transformer windings are shown.

Following the same concept used for the multiphase coupled-buck converter, an improved push-pull forward converter can be derived from the topology shown in Figure 3.41(b), by splitting the clamping capacitor Cs and modifying the interconnections of the primary windings and switches.

Figure 3.42 shows the implementation and the equivalent circuit of the proposed single-magnetic push-pull forward converter. The operation waveforms for both the

original and the improved push-pull forward converters are the same except the input current. In the improved push-pull forward converter, the input current is smooth, while the original one exhibits a pulsing input current. The smooth input current means that a built-in input filter exists in the improved push-pull forward converter. The built-in input filter is formed by the leakage inductance and the clamping capacitors.

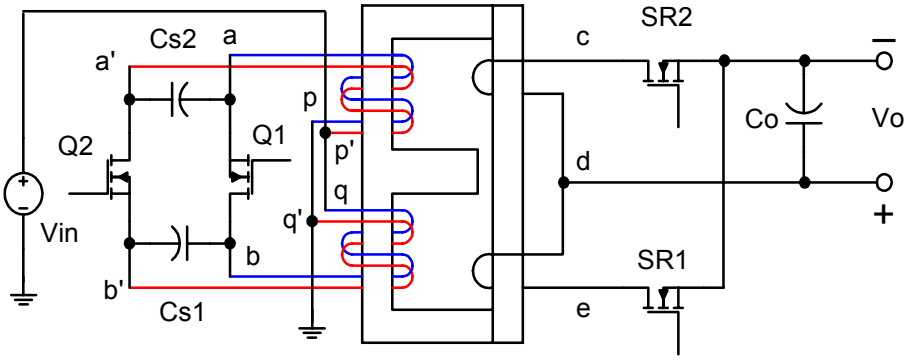

(a)

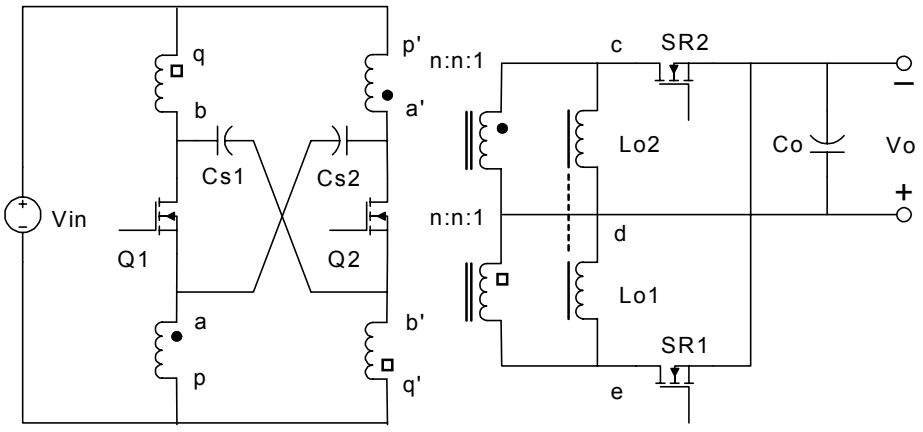

(b)

Figure 3.42. Push-pull forward converter with built-in filter: (a) implementation; and (b) equivalent circuit.

The same integrated magnetic structure is used for both the original and the improved push-pull forward converters. However, in the improved push-pull forward converter, the

suitable leakage inductance of the transformer's primary windings is utilized as the input filter inductor.

3.4.4.2. Winding Design for Built-in Filter

Two kinds of leakage inductances exist in the proposed integrated magnetic structure: One is between the primary and secondary windings, and the other is between the two primary windings. The primary-secondary leakage inductance (Lsp) must be minimized, since it causes parasitic ringing across the switching devices, decreases the effective duty cycle at the secondary, and impairs overall efficiency. The primary-primary leakage inductance (Lpp) is utilizes as the input filter inductance, therefore it has a suitable value if the input filter is fully integrated. In this section, the 2-D FEA simulation is used to find out some simple ways to minimize the primary-secondary leakage inductance (Lsp) and achieve a suitable level of primary-primary leakage inductance (Lpp).

Because of the small inductance requirements of multiphase VRMs, one turn can be used for the secondary windings. PCB winding and the planar cores can be used to reduce the profile of the power stage. With the PCB winding, the high-current termination at the secondary can be eliminated in order to improve the efficiency.

Figure 3.43 shows some possible winding arrangements. The red, blue and pink colors represent the first primary winding, the second primary winding and the secondary winding, respectively. Because the two primary windings are paralleled when the primary switches conduct, any difference in the leakage inductance of these two windings would

cause unequal currents to go through these windings and would thus impair efficiency. In this sense, the two primary windings should have a symmetrical layer arrangement.

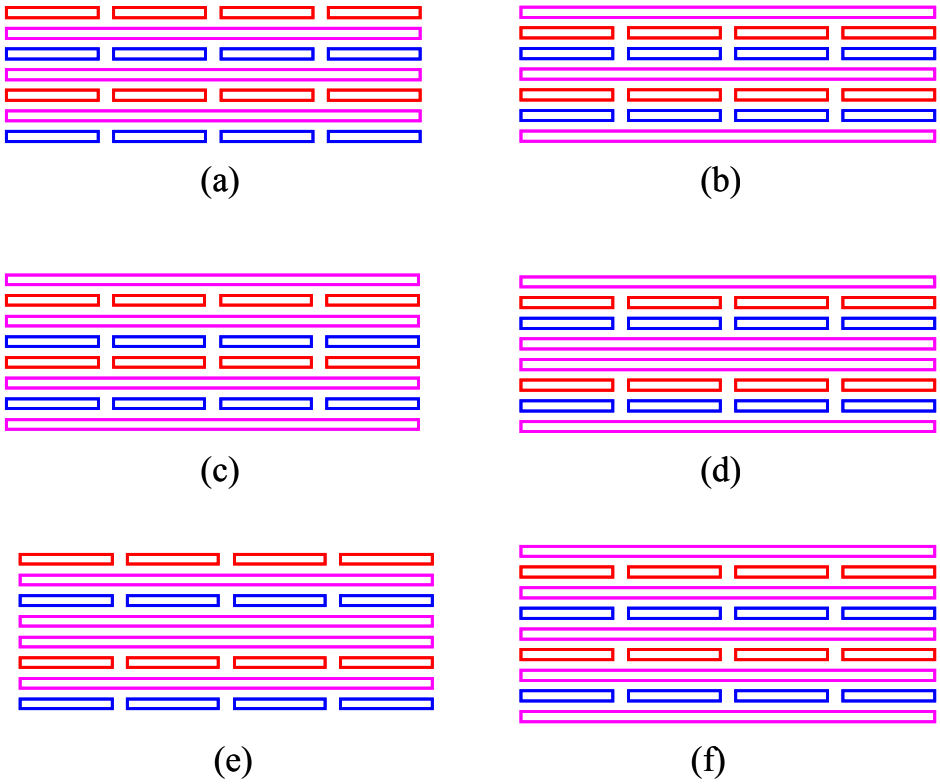

Figure 3.43. Winding arrangements: (a) seven layers (I), (b) seven layers (II), (c) eight layers (I), (d) eight layers (II), (e) eight layers (III), and (f) nine layers.

In this example, the dimensions of the E-I cores are based on the E32/6/20 and the PLT 32/20/3 from Philips. Each of the two primary windings has eight turns. Because of the limited width of the core window, each layer can only contain four turns of the primary windings. The two primary windings occupy four layers. The secondary winding has one turn with the remaining layers paralleled. Each copper layer of the windings is

two ounces. The thickness of the insulation layers between the windings is 200 um. Due to a limitation of the software, the winding currents can only be sinusoidal waves. Therefore, The fundamental component of the real winding currents is used. The frequency of the sinusoidal waves in the simulation is 100 kHz.

Figure 3.44 shows the primary-secondary leakage inductance (Lsp) and the corresponding AC resistances for different winding arrangements.

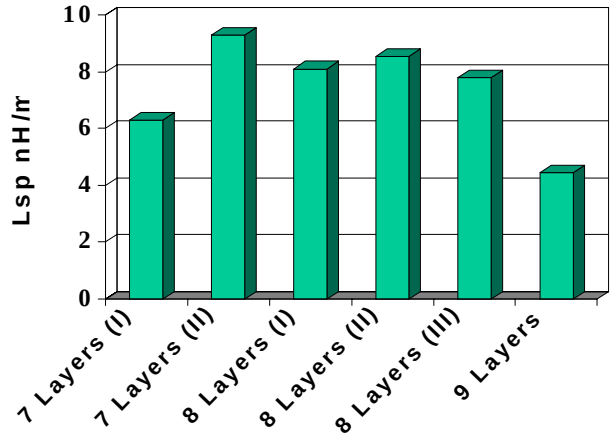

(a)

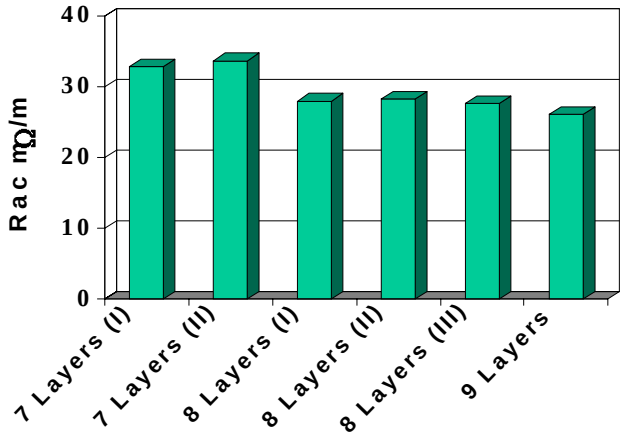

(b)

Figure 3.44. Simulation results: (a) the primary-secondary leakage inductance (Lsp); and (b) winding AC resistances (reflected to the secondary side).

As can be seen from Figure 3.44, fully interleaved windings are preferred to minimize both the primary-secondary leakage inductance (Lsp) and the AC resistances. Because of the required symmetrical-layer arrangement for the two primary windings, even layers cannot achieve the fully interleaved windings. Figure 3.44 also indicates that the more layers of fully interleaved windings there are, the lower the primary-secondary leakage inductance (Lsp) and the AC resistances will be. Therefore, fully interleaved odd windings should be used in order to minimize the primary-secondary leakage inductance.

The primary-primary leakage inductance (Lpp) is utilizes as the input filter inductance; therefore it has a suitable value if the input filter is fully integrated. Generally, the control of the leakage inductance is difficult and requires some special designs. However, the use of the PCB windings can offer some advantages in terms of controlling the leakage inductance.

Figure 3.45 shows a simple way to control the primary-primary leakage inductance, by interleaving the windings in different levels.

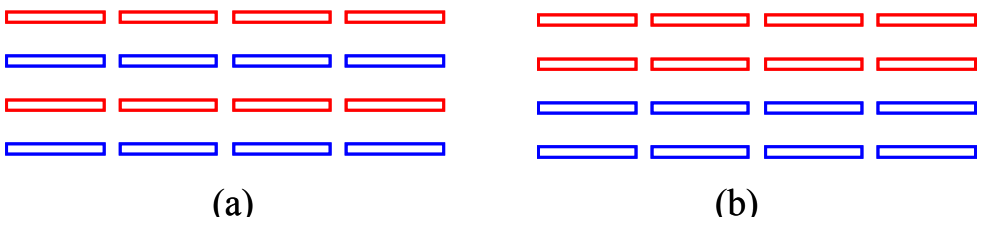

Figure 3.45. Controlling the leakage inductance by using different methods to interleave the windings.

Figure 3.46 shows the primary-primary leakage inductance (Lpp) and the corresponding AC resistances for Figure 3.45's winding arrangements.

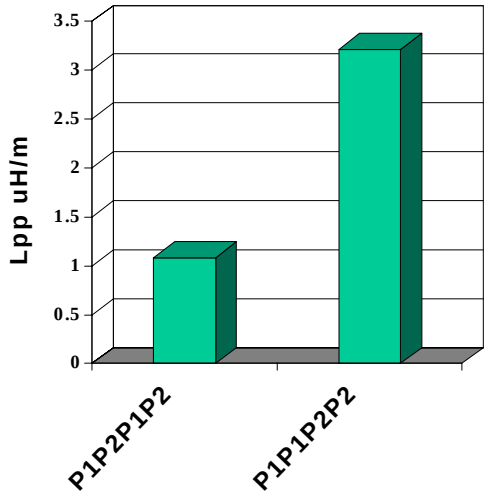

(a)

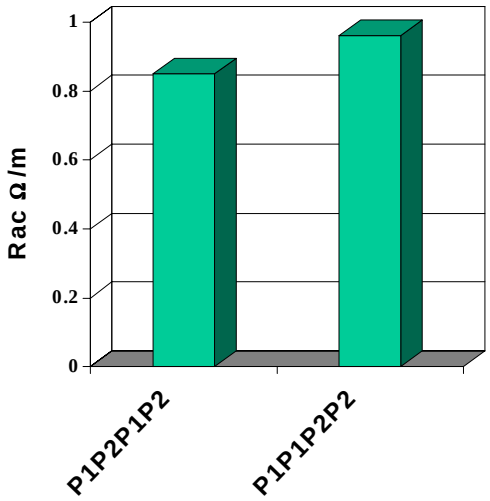

(b)

Figure 3.46. Simulation results for Figure 3.45's windings: (a) the primary-primary leakage inductance (Lpp); and (b) winding AC resistances (reflected to the primary side).

As can be seen from Figure 3.46, fully interleaving the windings gives the lowest primary-primary leakage inductance (Lpp) and the lowest AC resistances. By increasing the weakness of the winding interleaving, the primary-primary leakage inductance (Lpp) also increases. By interleaving the windings in different levels, the primary-primary leakage inductance (Lpp) can be controlled. However, the AC resistances also become larger as the leakage inductance increases. Certain tradeoffs have been made between the winding loss and the leakage inductance. The flexibility to control the leakage, as illustrated in Figure 3.45, is limited by the total number of available layers. For a small number of layers, the different interleaving configurations are very few. Therefore, this method is more suitable for a large number of layers.

Another method for controlling the leakage inductance is illustrated in Figure 3.47, without the above limitation. The idea is to adjust the overlap between the two windings. Figure 3.47(a) represents two fully overlapped windings, and Figure 3.47(b) represents two partially overlapped windings.

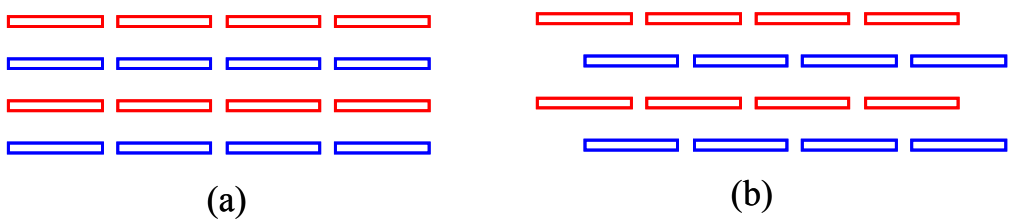

Figure 3.47. Controlling the leakage inductance by partially overlapping the windings.

Figure 3.48 shows the primary-primary leakage inductance (Lpp) and the corresponding AC resistances with zero, quarter and half shifts of the width of winding.

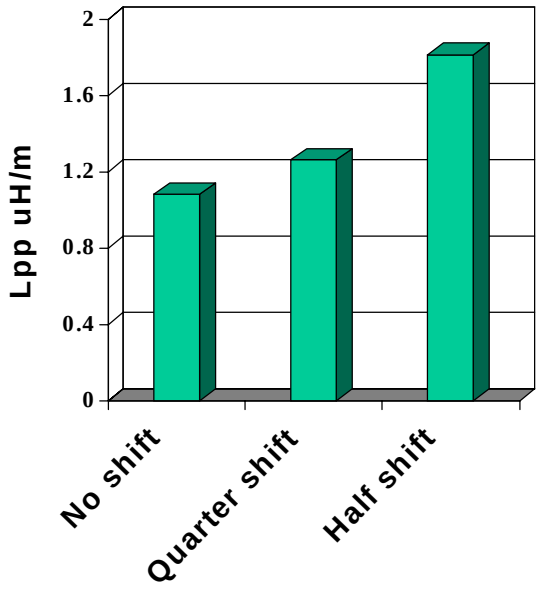

(a)

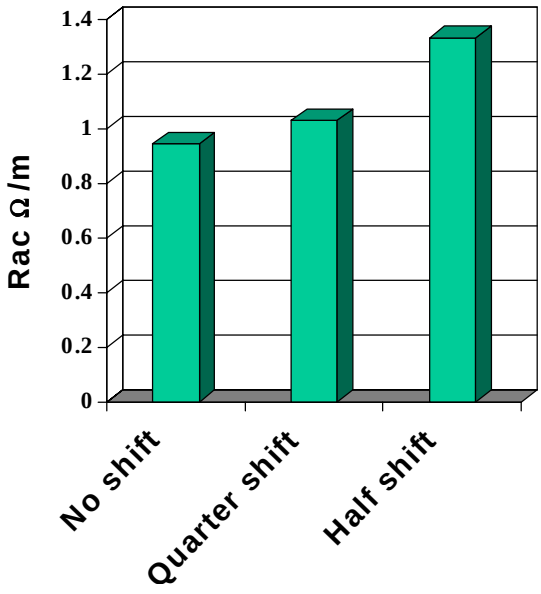

(b)

Figure 3.48. Simulation results for shifted windings: (a) the primary-primary leakage inductance (Lpp); and (b) winding AC resistances (reflected to the primary side).

As can be seen from Figure 3.48, with the increase of shifts (less overlapping), the primary-primary leakage inductance (Lpp) also increases. By adjusting the overlap between the two windings, the primary-primary leakage inductance (Lpp) can be controlled. The adjustment is continuous; therefore, any reasonable leakage inductance can be achieved. However, the AC resistances also become larger as the leakage inductance increases. Certain tradeoffs have been made between the winding loss and the leakage inductance.

3.4.4.3. Experimental Results

The single-magnetic push-pull forward VRM was developed with V_{IN} = 48 V, V_O = 1.2 V, I_O = 70 A, and F_S = 100 kHz. Each of the two primary switches uses PSMN035-150B (150 V, 35 mΩ) from Philips Semiconductor, and each of the two secondary switches uses 2 X STV160NF03L (30 V, 3 mΩ) from ST Microelectronics.

The magnetic core is a pair of E32-3F3 and PLT32-3F3 with a 10mil air gap in the center leg. The windings are built in a nine-layer 2oz PCB with four layers for the primary windings and five layers for the secondary winding. Each of the two primary windings has eight turns with four turns per layer. The secondary windings use a single turn with five layers paralleled.

The measured leakage inductance between the two primary windings is about 1.4 uH, which is used as the input filter inductor. The two clamping capacitors are each 3.3uF. Figure 3.49 shows a photograph of this 48V VRM prototype.

Figure 3.49. 48V VRM prototype using the single-magnetic push-pull forward converter.

Figure 3.50 shows the experimental waveforms at full load. With the integrated input filter, the input current is smooth in the improved push-pull forward converter.

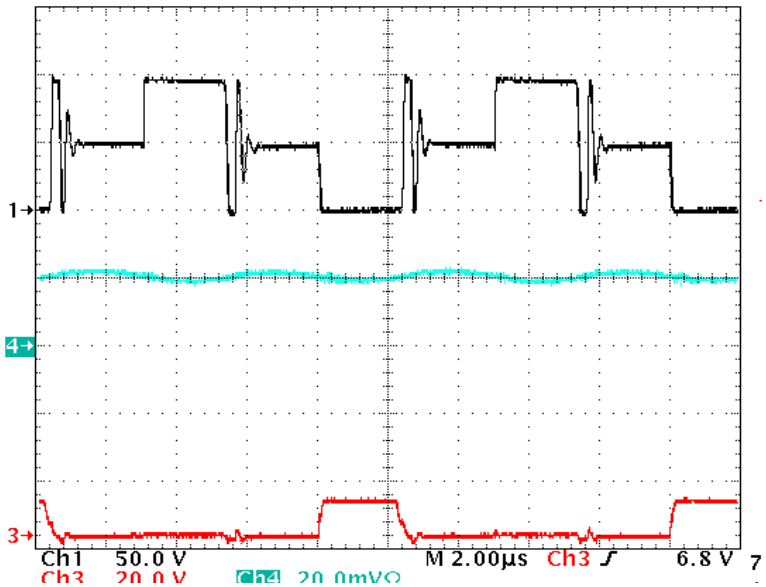

Figure 3.50. Experimental waveforms at full load for the single-magnetic push-pull forward converter: Vds (top), Iin (middle), and Vgs (bottom).

Figure 3.51 shows the measured efficiency. The improved push-pull forward converter achieves a 91% ceiling efficiency and an 85% full-load efficiency. Compared to the conventional push-pull converter, the improved push-pull forward converter has an efficiency improvement of more than 3%. Compared to the original push-pull forward converter, the integration of the input filter also helps improve the efficiency, especially at light load.

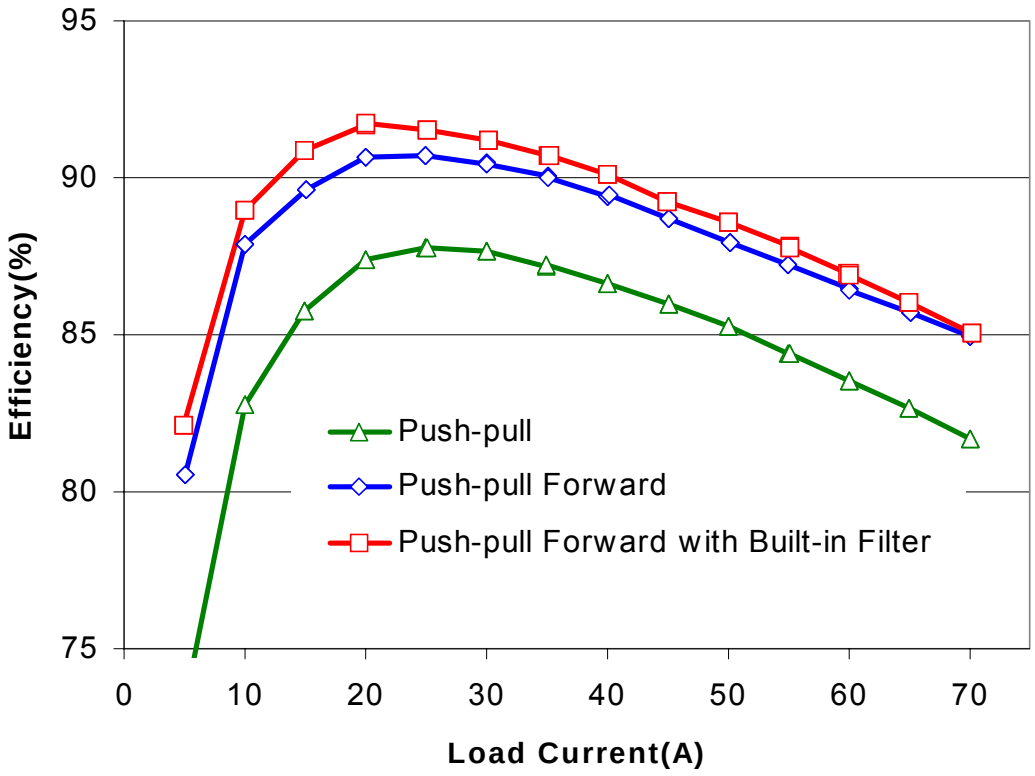

Figure 3.51. Measured power-stage efficiency for conventional push-pull, push-pull forward and push-pull forward converters.

3.5. SUMMARY

The use of integrated magnetic techniques in multiphase VRMs can reduce the number of magnetics and improve the efficiency. All the magnetic components can be integrated into a single core, in which the windings are wound around the center leg and the air gaps are placed on the two outer legs.

Studies show that the core structure of the integrated magnetics requires precise adjustment and is not mechanically stable. The existence of air gaps on the two outer legs also causes EMI issues. Large leakage inductance exists in the integrated magnetics, causing severe parasitic ringing, decreasing the duty cycle and impairing the efficiency.

An improved integrated magnetics has been proposed to solve these problems. In the proposed structure, all the windings are wound on the two outer legs, the core structure has an air gap in the center leg, and there are no air gaps in the two outer legs. This kind of core is easier to manufacture. The windings are physically located on the same legs. The interleaved winding technique can be used to minimize leakage inductance.

In the proposed integrated magnetics, the air gap in the center leg introduces coupling between the two output filter inductors. With the coupled output inductors, both the steady-state and dynamic performances of the multiphase VRMs can be improved. Another benefit of the proposed integrated magnetic structure is the flux ripple cancellation effect in the center leg. With the small flux ripples in the center leg, the core

loss there can be reduced. The fringe effect of the air gap becomes insignificant, and the winding loss can also be reduced.

Unlike conventional magnetic integrations, the input filter has also been integrated into the proposed structure. The input inductor is formed by the leakage inductance between the transformer's primary windings. This leakage inductance can be controlled by carefully designing the winding. With the proposed integrated magnetics, it is possible to use only a single magnetic core for the whole converter.